Research papers

Propagation of variability in climate projections within urban flood modelling: A multi-purpose impact analysis

Roberta Padulano [a,*], Guido Rianna [a], Pierfranco Costabile [b], Carmelina Costanzo [b], Giuseppe Del Giudice [c], Paola Mercogliano [a]

[a] Regional Models and geo-Hydrological Impacts Division, Fondazione Centro Euro-Mediterraneo sui Cambiamenti Climatici, Via Thomas Alva Edison, 81100 Caserta, Italy
[b] Department of Environmental Engineering, University of Calabria, via P. Bucci cubo 42/B, 87036 Rende (CS), Italy
[c] Department of Civil, Architectural and Environmental Engineering, University of Naples "Federico II", Via Claudio 21, 80125 Naples, Italy

ARTICLE INFO

ABSTRACT

Flooding is one of the most challenging weather-induced risks in urban areas. However, in a climate change perspective, significant gaps can still be observed in literature addressing the key role of rainfall input and related variability within urban flood impact models. The present research attempts to bridge this gap by investigating the effect of using a large ensemble of bias-corrected Euro-CORDEX climate projections on flood hazard estimations, with the goal of understanding the propagation of future climate variability in terms of flooding outputs for the urban environment. With this aim, a scenario analysis is performed for two return periods (10 and 200 years) building on nineteen climate projections for future horizon 2071–2100 under RCP 4.5 and 8.5 scenarios by means of CADDIES Caflood inundation model, using a test case in the City of Naples (Italy). Model outcomes are investigated and discussed in terms of relevant metrics and indicators available in literature targeting both general hazards, evaluated in terms of runoff volumes and flooded areas, and sectoral hazards, specified by a number of relevant literature hazard classifications. Modelling outcomes are analysed and normalised with respect to baseline values representing current climate conditions to emphasize potential impacts of climate change. Results show that flood features increase more slowly than rainfall, and the relationship between rainfall and flood increase is linear, with decreasing slope with increasing return period. Furthermore, the spread in rainfall input due to the use of different climate projections does not inflate through the impact modelling stages, albeit a dependence on the indicators used to model flood impacts can be observed. The outcomes of the research can be of aid to managers, designers and policy makers to understand the impacts of climate change in flood-prone urban areas and, in perspective, to adapt urban areas exploring the feasibility and effectiveness of solutions.

1. Introduction

Flooding is one of the most challenging weather-induced risks in urban areas, due both to the typically high exposures in terms of people, buildings and infrastructures (Ashley et al., 2005; Hlodversdottir et al., 2015; Zhao et al., 2019; Zhou et al., 2019; Kourtis and Tsihrintzis, 2021), and to the uncertainties lying in the modelling of the involved physical processes (Kaspersen et al., 2017; Li et al., 2019; Alves et al., 2020). The complexity of urban environments is so high that, according to the specific focus of the analysis, flood impacts are usually estimated either in general terms, quantifying the extent and magnitude of flooded areas

(which should be only the first step of flood impact assessments according to Hammond et al., 2015), or targeting specific sub-systems with tailored evaluations, such as stage-damage curves (He et al., 2020) and traffic disruption models (Forero-Ortiz et al., 2020; Kasmalkar et al., 2020). Detailed focus on the response of urban sub-systems is often coupled with simplified approaches for flood estimation: for instance, it has been argued that there still exists a gap in research in giving sufficient consideration to the changes in rainfall at the urban level due to the effects of climate change, and its direct effect on the change in vulnerability of transport systems (metro network, specifically) at the local, regional and global scales (Madsen et al., 2014; Forero-Ortiz et al.,

2020).

In the framework of urban flood modelling, accuracy and reliability of results are deeply affected by the amount and detail of data required by the adopted modelling tool (Cao et al., 2020; Costabile et al., 2021), and by the spatial resolutions involved (Guidolin et al., 2016; de Almeida et al., 2018), as well as by a general unavailability of flood impacts observations suitable for validation purposes (Wang et al., 2018; Macchione et al., 2019; Cao et al., 2020). In this perspective, meanwhile current literature is proactive in exploiting novel modelling tools able to reproduce flood features in the most accurate way (Wu et al., 2020), simplified models are particularly appreciated for scenario analysis (Löwe et al., 2017; Palla et al., 2018; Webber et al., 2019a; 2019b; Cao et al., 2020). In this case, the focus is the effect of a single or a set of modelling parameters, which is investigated with a comparative analysis in spite of the accuracy of each simulation. This approach is particularly feasible, for instance, for selection, screening, or viability assessments of drainage solutions at pre-design stage.

Scenario analysis is particularly suitable to investigate the possible impacts of climate change, whose estimation should account for the uncertainties lying in the adoption of different climate simulation chains, as prescribed by the 5th Assessment Report (AR5) of the Intergovernmental Panel on Climate Change (IPCC, 2014). According to IPCC (2014), the frequency and/or magnitude of precipitation events could be greatly impacted by the expected climate change (Donat et al., 2016; Papalexiou and Montanari, 2019; Hosseinzadehtalaei et al., 2020; Tu et al., 2020) primarily due to the increase in temperature, entailing an increase in the atmospheric moisture retention capability. However, the effect of climate change on the rainfall regime of local areas is not straightforward, but deeply depends on the particular local features such as latitude, topography, distance from the coast. In this regard, Mediterranean area is recognized as a hot spot for climate change, since climate projections are consistent in providing future drying trends that could exacerbate social and geopolitical tensions in severely water-stressed regions such as North Africa and Middle East (Seager et al., 2019; Tuel and Eltahir, 2020). Due to the very complex geomorphological features of the area, the adoption of downscaling (statistical or dynamical) approaches is required to properly assess the atmospheric patterns and the associated variations under climate change (Zollo et al., 2016; Bucchignani et al., 2018; Jacob et al., 2020). The complexity of climate modelling, along with the identification of several possible future socio-economic and greenhouse gas concentration scenarios ("Representative Concentration Pathways", RCP), acting as the main forcing, has generated a large number of climate projections for the next decades, providing different possible scenarios for the evolution of extreme rainfall regime of local areas (Reder et al., 2018; Padulano et al., 2019). As particularly concerns pluvial flooding of urban environments, current scientific literature provides only a limited number of examples of impact analyses accounting for an ensemble of climate projections, as described below. The main difficulties mostly lie in the very large computational and storage requirements needed to deal with climate projections (even more so considering the continuously increasing number of climate simulations made available to the public, such as those included in the Euro-CORDEX initiative), in the assumptions and post-processing needed by those climate data to be made suitable for impact analyses, particularly in terms of spatial and temporal scales (Maraun et al., 2010; Willems and Vrac, 2011; Arnbjerg-Nielsen et al., 2013), and in the additional complexity required by climate models to correctly capture the spatiotemporal dynamics of urban climate (Ban et al., 2021). Nevertheless, currently available spatial resolutions from raw climate models often prevent a reliable reproduction of precipitation patterns at very fine spatial and temporal scales. Sperotto et al. (2016) provided a methodology for pluvial flood risk assessment in the City of Venice (Italy) in a context of climate change, considering the results of a single raw climate projection under the RCP 8.5 scenario. Kaspersen et al. (2017) considered an ensemble of ten Euro-CORDEX bias-adjusted climate projections under RCP 4.5 and

RCP 8.5 for a number of European cities. Pregnolato et al. (2017) provided a framework for risk assessment due to traffic disruption, simulating a climate change scenario in Newcastle (UK) by means of a synthetic rainfall uplift assessment as provided by Dale et al. (2015) for the UK. Kaspersen and Halsnæs (2017) investigated the effect of climate change on a number of urban sub-systems (buildings, roads, human health, cultural assets) in the city of Odense (Denmark) by using one single climate simulation chain under the RCP 4.5 and RCP 8.5 scenarios, as well as the global +6° scenario. Martinez-Gomariz et al. (2019) provided a wide methodology for the estimation of flood risk targeting pedestrian and vehicular traffic in Badalona (Spain), making use of one single climate projection included in Euro-CORDEX under RCP 8.5. Zhou et al. (2019) investigated the effect of climate change on flooding for a major city in Northern China using an ensemble of low-resolution bias-adjusted Global Climate Models (GCMs) under RCP 2.6 and RCP 8.5. Gusain et al. (2020) considered six GCMs, downscaled from their native low resolution and suitably bias-adjusted in terms of both precipitation and temperature, as input for hydrodynamic modelling and hazard analysis; the focus is on a very large -scale catchment with the main objective of building priority maps for flooded villages. Such a State-of-the-Art shows that, on one hand, the variability of climate modelling is seldom considered, since only a limited number of climate projections are included in the analysis (or, alternatively, a synthetic approach is preferred by means of the ensemble mean or relevant percentiles); on the other hand, the effects of such a variability are usually not the main focus of the analysis, as they are often overlapped with other sources of uncertainty. In the above-mentioned literature, the more specific is the target of the analysis, for instance requiring additional post-processing or modelling steps, the narrower the ensemble of climate projections or scenarios adopted.

The proposed research attempts to bridge the gap between climate change modelling and urban flooding analysis by adopting a large ensemble of climate projections as input for urban flood modelling. The goal of the analysis is that of understanding the propagation of climate variabilities in terms of flooding outputs, with the particular purpose of estimating the impacts on a number of relevant urban sub-systems. With this aim, nineteen climate projections, suitably bias-adjusted, will be considered among those made available by the Euro-CORDEX initiative, and used as input for a grid-based inundation model (Guidolin et al., 2016). Different metrics and indicators will be used to analyse flood results, providing information suitable for multi-purpose and multi-sectoral impact analysis, and tailored information to quantify the response of urban services with respect to any changes in rainfall intensity, as those possibly caused by climate change. Finally, results of the involved modelling steps will be overlooked with a bird-eye perspective to understand the overall propagation of the variability in climate change projections throughout the system.

The rest of the paper is organized as follows. First, for each stage of the analysis (extreme climate modelling, flood inundation modelling, flood hazard evaluation) an overview is presented to correctly position the research in the field literature and a full description of the adopted methodology is provided in order to highlight the rationale behind the choices made. Then, a case study is presented and described, along with relevant topographic and climate in situ data. Successively, results of the consecutive modelling steps for the case study are presented. Finally, a discussion of the impacts and limitations of the research is provided, and relevant conclusions are drawn.

2. Rationale and methodology

As Fig. 1 shows, the workflow of the research is structured in three main modelling modules, namely (i) the climate changes module, (ii) the flood inundation module and (iii) the flood hazard module. The first module builds on locally designed Intensity – Duration – Frequency (IDF) curves and spatially distributed rainfall datasets in order to identify the impacts of climate changes on the local extreme rainfall regime,
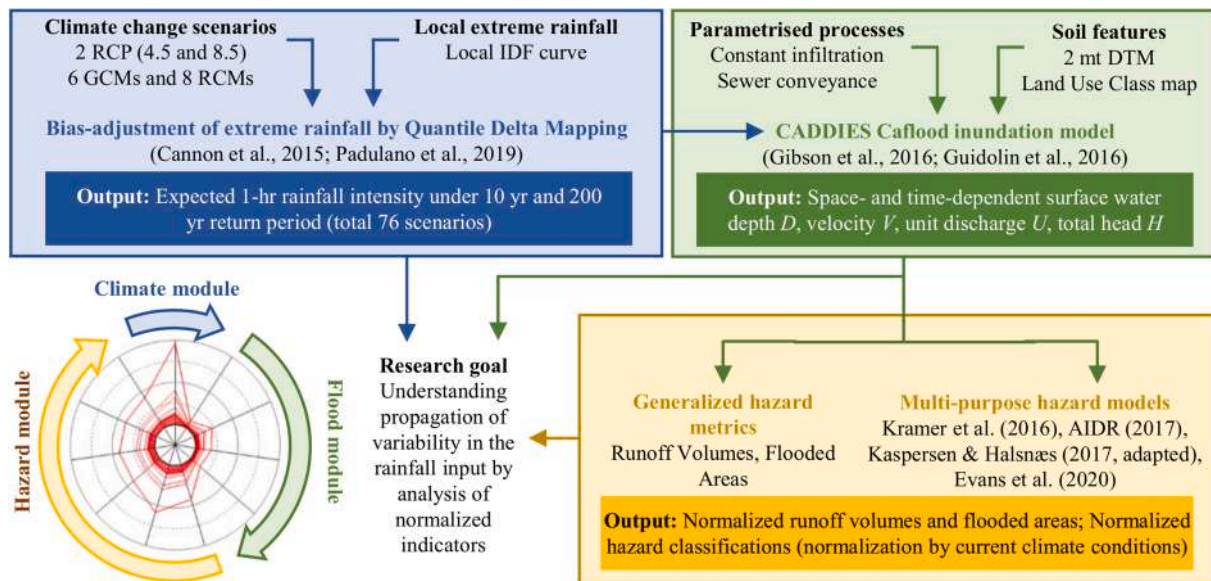
Fig. 1. Workflow and Impact Simulation Chain. Climate module (blue) identifies rainfall scenarios used as input for the Flood module (green), whose results are used to evaluate selected metrics, models and indicators in the Hazard module (yellow). Outcomes of single steps can be used to map and visualize propagation of variability: each line of the radar graph maps the outcomes of each simulation starting from rainfall intensity and ending in hazard estimations. (For interpretation of the references to colour in this figure legend, the reader is referred to the web version of this article.)

relying on cutting-edge bias adjustment techniques. The outcomes of the climate module are the main input of the second module, which relies on a grid-based flood inundation model with a degree of simplification acceptable for scenario analysis. The third module translates flood features into relevant metrics for flood hazard estimations to investigate the potential effects of climate changes on flood risk conditions of urban environments. The final step consists of integrating the results of the preceding modules to understand how the variability in the rainfall input due to the use of multiple climate projections propagates throughout the impact modelling system.

2.1. Climate change module

Raw daily precipitation data are returned by nineteen climate experiments included in the Euro-CORDEX ensemble (https://www.euro-cordex.net/), where Global Climate Models/Earth System Models (GCMs/ECMs) included in the 5th Coupled Model Intercomparison Project (CMIP5) are dynamically downscaled by using Regional Climate Models (RCMs) over a domain centred on Europe with a horizontal resolution of $0.11°$ ($\simeq 12$ km). Currently, Euro-CORDEX is the most used ensemble for impact analyses related to extreme climate, due to the high number of included projections and to the added value in reproducing climate dynamics with respect to ensembles with lower horizontal resolutions (Jacob et al., 2020). However, although the increase in spatial resolution due to downscaling provides an improvement in the characterization of regional weather patterns, structural uncertainties persist due, for instance, to the epistemic uncertainty in the knowledge of climate systems as well as to the modelling uncertainty related, for example, to the computationally allowable spatial resolutions and associated needed parametrizations for sub-grid processes. Under such constraints, the recognized biases in the different climate experiments prevent the adoption of raw climate outputs as inputs for impact analysis, especially for extreme events, where sub-grid processes could play a relevant role. To deal with these issues, in recent years, several statistical approaches have been proposed to reduce the biases, assumed as systematic, by adjusting climate outputs towards observed weather data used as reference over a common time period. Padulano et al. (2019) proposed an innovative approach where the bias adjustment procedure is directly applied on IDF curves, which constitute the main instrument

to deal with extreme rainfall (Chow et al., 1988; WMO, 2009; Arnbjerg-Nielsen et al., 2013).

The present research builds on the methodology proposed by Padulano et al. (2019) which allows for the estimation of novel Intensity-Duration-Frequency curves updated to account for the effect of climate changes, relying on Quantile Delta Mapping (QDM; Cannonet al., 2015) for bias adjustment. QDM is a parametric bias correction technique particularly appreciated to preserve the climate signal at all probability levels, and especially for the extremes. Advantages are counterbalanced by the larger computational effort required to fit probability distribution models to the observations as well as to model simulation results. In short, QDM consists of scaling raw projected values by means of a probability-dependent bias, estimated as the ratio of observed to simulated (for the reference period) quantiles for the same probability level (or return period T). The governing formula for QDM, applied to the annual maximum daily rainfall depth h_d, in (mm), is shown in Equation (1).

$$h_{d,bc}(T) = h_{d,proj}(T) \cdot \frac{\Phi_{obs}^{-1}(T)}{\Phi_{curr}^{-1}(T)} \tag{1}$$

where subscripts *obs*, *curr* and *proj* point to the annual maximum precipitation depth samples coming from the observations (or, alternatively, from a locally available IDF curve) for the reference period, from the model results for the same reference period and from the model results for a future horizon, respectively; subscript *bc* points to the final bias-corrected values; Φ^{-1} stands for the inverse cumulative distribution of daily precipitation depths. All terms refer to the same probability level, or return period T. In order to obtain IDF curves for sub-daily rainfall durations, the storm index approach is applied (Viglione et al., 2007), separately investigating the empirical dependence of mean annual maxima on rainfall duration and the probabilistic distribution of growth coefficients. For the first term, the same dependence estimated from the observations (or, alternatively, from a locally available IDF curve) is retained, assuming that it does not experience modifications in its structure due to climate changes. For the second term, results obtained from daily precipitation values are extended to all the durations, under the assumption that annual maxima of daily rainfall are closely related to the annual maxima for a duration of 24 h. Accounting for

those assumptions, as demonstrated by Padulano et al. (2019) Eq. (1) can be rewritten as:

$$h_{bc}(t,T) = h_{obs}(t,T) \cdot \Delta_m(T) \tag{2}$$

where t points to any rainfall duration, in [h], and $h_{obs}(t,T)$ coincides with the observed (or estimated by current locally available IDF curves) annual maximum rainfall depth for any rainfall duration t and return period T. Δ_m is the scaling factor representing the effects of climate changes as provided by a climate projection m (for example, one within a larger ensemble), expressed as a function of return period T.

In Padulano et al. (2019), an ensemble of nineteen climate projections was used, and results were provided only in terms of ensemble mean and standard deviation. Instead, in the present research, the single members of the adopted ensemble of climate projections are retained individually, in order to investigate the propagation of this source of variability through flood modelling, and to better understand the effects in terms of flood features and flood hazard. This also complies with recent literature, suggesting that dealing with climate projections as they were independent realizations of a random variable (i.e. analysing the ensemble as a statistical sample, with a central value and a standard deviation, Tebaldi et al., 2005) could be questioned because the different GCMs/RCMs pairs often share assumptions and parametrizations, possibly violating the assumption of statistical independence (Sanderson and Knutti, 2012; Christiansen, 2020). In other words, although results provided by an ensemble of climate projections could cluster in a narrow space (as will be demonstrated in the present research for the investigated case study), this does not mean that single climate projections positioning far from the cluster should be considered as outliers (namely, less probable).

2.2. Flood inundation module

CADDIES Caflood is a flood modelling software relying on Cellular Automata (CA) and based on a square regular grid and Von Neumann neighbourhood (Ghimire et al., 2013; Gibson et al., 2016). This model employs simple transition rules and a weight-based system rather than Shallow Water Equations to resolve the flow movement, minimising the need for solving computationally expensive algorithms while maintaining high accuracy (Cao et al., 2020). The simplified features result in significantly improved modelling efficiency, ensuring reliable simulated water depths and velocities, with model run times up to 8 times faster than tested benchmark models for real-world applications (Guidolin et al., 2016).

Caflood is able to account for spatially and temporally variant rainfall intensities and infiltration rates, which must be manually fed by users as time series; the main outputs consist of spatially and temporally distributed water depths and flow velocities. The computational speed increase (translating in no dramatic computational requirements) is counterbalanced by the simplified representation of several underlying physical processes (Webber et al., 2019b), such as the effect of an artificial drainage network or the positioning of drainage interventions, that can only be simulated through local cell water balance and roughness parameters. Such a degree of simplification makes Caflood particularly useful for pre-design evaluations and scenario analysis (Webber at al., 2019a; 2019b; Cao et al., 2020), since at this stage no detailed data and information over the investigated areas are usually available; moreover, Caflood was found to reproduce observations with fair accuracy despite the simplifying assumptions (Wang et al., 2018). In particular, the simplified representation of sewer system can be considered feasible and consistent with the usually poor availability of related data (e.g. location and size of sewers). Other modelling tools share the same approach, setting the infiltration rate due to the stormwater system to a reference value, chosen arbitrarily (Cao et al., 2020) or equal to the sewer network design rainfall (Kaspersen et al., 2017). The code has been extensively validated using common benchmarks for flood propagation software

packages (Guidolin et al., 2016), although only a limited number of test cases involved purely pluvial flooding conditions.

2.3. Flood hazard module

In case of extreme rainfall in urban contexts, a cascade of adverse consequences can be identified consisting of the rainfall-runoff transformation (the flood) and the interaction with urban sub-systems such as buildings, infrastructure, and people. In this perspective, different levels of hazard can be identified stemming from different questions, such as: (i) how does the urban environment as a whole respond to extreme rainfall? and (ii) how does a specific urban sub-system respond to flooding? In a climate change perspective, such questions can be further attuned as (i) *to what extent do flooding conditions change when extreme rainfall changes?* and (ii) *to what extent does a service keep a certain operational level despite climate changes?* Answering the first question requires modelling the rainfall-runoff transformation process, in order to understand changes e.g. in flooded areas, flood depths and stormwater volumes; this will be hereafter referred to as "cumulative hazard". Answering the second question implies accounting for the features of the investigated sub-system, such as the transport network or pedestrian circulation, and their interaction with flooding features; this will be hereafter referred to as "operational hazard". Although operational hazard can be regarded as a downstream effect of cumulative hazard, rainfall-runoff transformation models often include some urban sub-systems showing a physical interaction with rainfall, such as roads, buildings, or green areas. Given the complexity of modelling both processes, a useful approach can consist in deriving from model simulations indicators and criteria suitable to be used as input for operational hazard estimation of the largest possible number of urban services and sub-systems.

In the present paper, cumulative and operational hazards are investigated exploiting quantities and indicators commonly adopted in the field of flood risk, deployed in hazard classifications targeting one or multiple sectors, as described below. The simplest variables are water depth D (mm) and velocity V (m/s); other variables such as flood duration will not be considered although they may have an effect on urban risks (Luu et al., 2018). D and V are the raw output of flood modelling, typically adopted to compare the outcomes of different scenarios or different modelling approaches/strategies/tools, when the focus is on the rainfall-runoff transformation. Indeed, flood estimations focusing on flood model comparisons (e.g. Bermúdez et al., 2018), on the performance of flood adaptation measures (Webber et al., 2019a; 2019b) or on the impact of climate changes (Kaspersen et al., 2017) typically compare baseline to updated scenarios by only means of water depth D, or depth-related variables such as flooded areas or flood volumes. In such cases, different arbitrary classes for D can be used according to the experienced variability interval, ranging from a dry/wet threshold, usually set to 1 cm (Bermúdez et al., 2018), 5 cm (Kaspersen et al., 2017; Palla et al., 2018; Mei et al., 2020) or 10 cm (Singh et al., 2018) to a maximum value which is deeply affected by the local extreme rainfall regime and topography, but mostly by the proximity to an open drainage/river channel which usually causes larger flow features. Depth classes can be set arbitrarily by inspecting flood outcomes (Arrighi et al., 2019; Li et al., 2019; He et al. 2020; Tanaka et al., 2020); natural breaks can be used (Sperotto et al., 2016) as well as deciles obtained inspecting the occurrence frequency of water depth within a flood map (Cao et al., 2020; Papilloud et al., 2020); stretched values can also be adopted (Chen et al., 2018, Costabile et al., 2020a). Water depth can also be used directly for hazard classification: Mei et al. (2020) suggested six hazard classes, the first in the range $D = 5–10$ cm, with incremental steps of 10 cm related to different levels of damage; Cao et al. (2020) proposed three hazard classes, starting from zero depth, with incremental steps of 15 cm; Singh et al. (2018) classified four flood severity levels as "no flood" (0–10 cm), "minor flood" (10–50 cm), "moderate flood" (50–100 cm) and "major flood" (>100 cm); a similar classification is proposed by

Pregnolato et al. (2017) but with lower thresholds (10, 20, 30 cm).

Water depth D can provide focus on some operational hazards, such as flood hazard for the transport services or buildings, feeding threshold values for binary classifications identifying affected/not affected assets. For instance, Kramer et al. (2016) suggested that roads inundated with a water depth of at least 50 cm should be closed for civil traffic; for Arrighi et al. (2019) the threshold can be lowered to 30 cm; Kaspersen and Halsnæs (2017) reported thresholds of 20 cm for buildings, 5 cm for basements, roads and railways, 0.3 cm for health (health issues are assumed to occur as soon as polluted storm water enters basements), 20 cm for historical/cultural assets. Incremental threshold values or hazard classes can be derived by stage-damage curves such as those provided by Van Ootegem et al. (2015) for buildings, basements and related content.

Water depth D (alone or coupled with velocity-related Froude number Fr) is the main input of many investigations focused on the reduction in vehicle speed due to rainfall, considered as one of the main sources of traffic disruption (Pregnolato et al., 2017; Evans et al., 2020) as well as for the evaluation of flood risk for pedestrians and parked vehicles (Arrighi et al., 2019; Bocanegra et al., 2018; Martínez-Gomariz et al., 2019). Risk classifications can be successively derived based on the number of affected roads, people or vehicles. Water depth D and velocity V (often in terms of their combination $U = V \times D$ (m²/s) known as "unit discharge") feed a large number of hazard classifications targeting pedestrians (Russo et al., 2013) and vehicles (Bocanegra et al., 2018); a relevant example is the hazard classification proposed by the Australian Institute for Disaster Resilience (AIDR, 2017; Costabile et al., 2020a), identifying six hazard classes each relevant for a specific asset (children, elderly people, vehicles, buildings). The total head $H = D + V^2/2g$ is also adopted by Kramer et al. (2016) for flood hazard classification, compared to a threshold of 30 cm and 60 cm for the safety of passenger cars and emergency vehicles, respectively.

In the present paper, different indicators and classifications will be adopted in order to understand the impact of climate changes at different return periods on a wide variety of outcomes targeting both cumulative and operational hazard (Table 1) considered interesting for the case study. First, a traffic-oriented hazard classification will be adopted in accordance with Evans et al. (2020), fed by water depth D (hazard model #1). Second, the well-known U-based hazard classification provided by AIDR (2017) will be adopted, targeting multiple assets for integrated risk assessment (hazard model #2). Third, D will feed the threshold-based classification provided by Kaspersen and Halsnæs (2017), again allowing for integrated risk assessment (hazard model #3); however, the health-related threshold was removed to keep consistency with the wet/dry threshold of 1 cm. Finally, the classification based on total head H (Kramer et al., 2016) will be considered as an alternative to the AIDR classification combining depth and velocity information (hazard model #4).

Prior to hazard evaluations, two additional lumped indicators (labelled "Runoff Volume Index", RVI, in m³, and "Flooded Area Index", FAI, in %) will be analysed which aggregate information at the watershed level:

$$RVI = \sum_{i=1}^{N} w_i \bullet D_i \bullet A_i \tag{3}$$

$$FAI = \frac{1}{S_{tot}} \bullet \sum_{i=1}^{N} w_i \bullet A_i \tag{4}$$

where S_{tot} is the total extent of the study area, N is the number of cells in the investigated area, A_i is the cell size, D_i is the water depth in the cell, and w_i is a binary classificator assuming 0 value when D_i is lower than a wet/dry threshold (which is set to a value of 1 cm), 1 otherwise. In the present research, both RVI and FAI are only evaluated under peak conditions, identified by subscript p. In peak conditions each location of the case study attains its maximum water depth or velocity value experienced during the flood event (which could not be concurrent): in other

Table 1
Flood hazard models.

Hazard model	Flood metric (reference)	Hazard class	Class ranges	Class description
#1	D Evans et al. (2020)	H3	≥ 30 cm	high hazard (MAS[a] = 0, road closed)
		H2	$10 - 30$ cm	medium hazard (MAS[a] = 20 km/h)
		H1	< 10 cm	low hazard (MAS[a] = road speed limit)
#2	$U = V \cdot D$ AIDR (2017)	H6	>4 m²/s	unsafe for people, vehicles and buildings (failure)
		H5	≤ 4 m²/s (D[b] ≤ 4 m, V[b] ≤ 4 m/s)	unsafe for people, vehicles and buildings (damage)
		H4	≤ 1 m²/s ($D \leq 1.2$ m, $V \leq 2$ m/s)	unsafe for people and vehicles
		H3	≤ 0.6 m²/s ($D \leq 1.2$ m, $V \leq 2$ m/s)	unsafe for vehicles, children and the elderly
		H2	≤ 0.6 m²/s ($D \leq 0.5$ m, $V \leq 2$ m/s)	unsafe for small vehicles
		H1	<0.3 m²/s ($D < 0.3$ m, $V < 2$ m/s)	generally safe
#3	D Kaspersen & Halsnæs (2017)	H3	≥ 20 cm	unsafe for health, basements, roads, railways, buildings and historical/cultural assets
		H2	≥ 5 cm, < 20 cm	unsafe for health, basements, roads and railways
		H1	< 5 cm	generally safe
#4	$H = D + V^2/2g$ Kramer et al. (2016)	H3	≥ 60 cm	high hazard for passenger cars and emergency vehicles
		H2	$30 - 60$ cm	high hazard for passenger cars
		H1	< 30 cm	low hazard

[a] MAS = Maximum Allowable Speed of vehicles.
[b] Limiting water depth and velocity.

words, peak conditions do not correspond to a specific instant of the flood event, but they maximize criticality for every location of the investigated area. Given their extremely aggregated nature, those indicators are only suitable for cumulative hazard estimations, and they can be used for quick preliminary understanding and comparison among different scenario outcomes.

Peak conditions are also used for the evaluation of hazard models in Table 1: with this aim, the peak values of D, U and H are needed. The outcomes of hazard models in Table 1 are represented by the "Area Within the Class" (AWC) metric, expressed as a percentage of the inundable area of the case study, in other words comparing the area extent where the considered indicator is within a range of predetermined values across multiple scenarios. This approach has the main disadvantage of not accounting for the exact location of hazardous places in the study area; however, it was preferred to a cell-by-cell comparison due to the large number of scenarios to be simulated. Notice that the sum of AWC across the classes of each hazard model equals FAI_p.

3. Case study

Fuorigrotta is one of the administrative units of the City of Naples, located in the western part of the city (Fig. 2). The pilot area chosen for the analysis is 2.1 km² wide and it roughly coincides with the
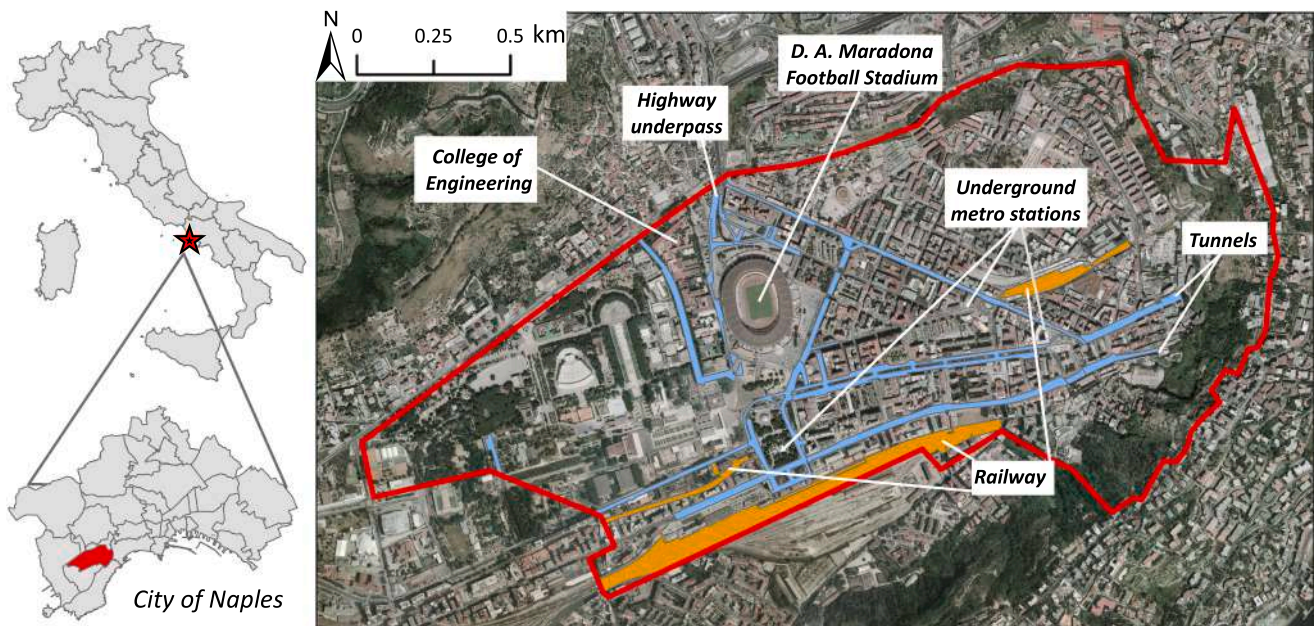
Fig. 2. Case study location and strategic assets (simulated domain in red, main roads in blue, railroads in orange). (For interpretation of the references to colour in this figure legend, the reader is referred to the web version of this article.)

stormwater drainage catchment serving the neighbourhood, which, in turn, is part of the complex and stratified combined sewer system of the City. The pilot area is located along the edges of the "Campi Flegrei" volcanic system: as such, it can be described as a flat basin with steep edges on the North-Eastern side, gently degrading towards the sea in

South-West direction (Fig. 2). Due to its peculiar topographic features, the drainage efficiency of the sewer system in the area has always been limited, and a large number of enhancements, retrofitting and extraordinary maintenance interventions have been proposed. The main concerns mostly regard the accumulation of surface runoff due to the very
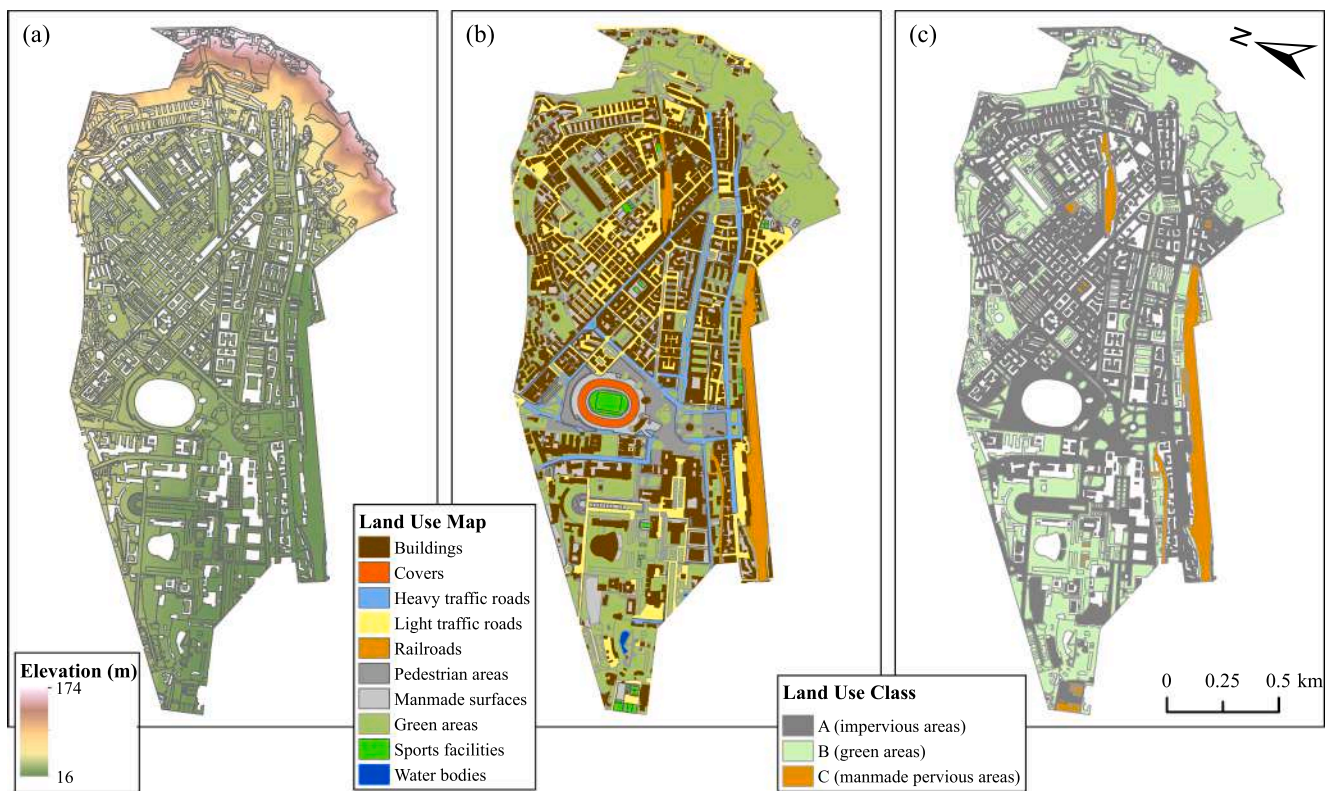

Fig. 3. (a) Digital Elevation Model; (b) Land Use Map; (c) Land Use classification of Fuorigrotta (NA). North arrow and scale bar refer to all panels. Data available at http://sit.cittametropolitana.na.it/lidar.html.

mild slopes in the central part of the pilot area, which, along with the overall poor maintenance conditions of gutters and drains, makes the storm water collection difficult.

All the above-mentioned issues have a deep influence on the rainfall-runoff transformation, exacerbating the flood hazard conditions of the area. In turn, flood risks are even more relevant considering the high exposure levels. The census particles (dated 2011) highlight the residential purpose of the pilot area, with a population of about 40′000 and still growing, and a number of highly relevant strategic assets such as the football stadium, with all the satellite economic activities, the railway infrastructure for public transport (both local and extra-urban, with a large number of underground stations), and the road network, which is characterized by a large number of high-traffic routes (also in underpasses and tunnels) connecting the area to the adjacent neighbourhoods and to the highway. Among all the above-mentioned assets (Fig. 3), the transport and road infrastructures proved to be the most vulnerable to pluvial flooding, with cascading indirect damages due to service disruption caused by traffic jams, potholes and railroad flooding, limiting mobility both within the area and towards the city economical/business centre. Relevant service disruptions can be observed both for small and for large return periods: an example of this can be found in the very large underpass at the highway exit, which is closed at every rainfall event as a precautionary measure, even for small rainfall intensities, with severe consequences for traffic. Moreover, damages to underground facilities, such as metro stations, but also garages and basements, are often experienced. For those reasons, this pilot area can be considered particularly interesting for pluvial flooding analysis, and especially in a context of climate change, in order to assess and map current and future hazard/risk conditions, as well as to plan adaptation strategies and measures.

3.1. Topographic data and land use maps

Different panels in Fig. 3 show the pilot area information that is needed for the modelling process, namely: (i) a LiDar-based Digital Terrain Model (http://sit.cittametropolitana.na.it/lidar.html) providing soil elevation with a native horizontal resolution of 1 m, remapped at a final resolution of 2 m, considered suitable for pluvial flooding analyses (Wang et al., 2018) and post-processed to remove building footprints; (ii) a Land Use classification, derived from merging different Land Use/Land Cover labels according to their surface drainage properties ("impervious areas", such as roads and pedestrian areas; "green areas"; "manmade pervious areas", including railroads and sports facilities). Land Use classes were assigned different roughness and infiltration rates consistently with Wang et al. (2018), considering, for the impervious areas, an infiltration rate coincident with the design extreme rainfall value for the sewer system with a return period of 2 years, accounting at the same time for the sewer design return period (usually < 10 years) and for the observed poor maintenance conditions. Moreover, infiltration rates for green areas were differentiated according to slope referring to the fine sandy loam soil texture, as suggested by Kaspersen et al.

(2017). Table 2 shows roughness and infiltration rate values for different Land Use classes and slopes; it should be noted that the "infiltration" label is used consistently with software notation and related literature (e.g. Wang et al., 2018), albeit it represents parametrized processes such as infiltration through green areas and sewer conveyance through drain inlets.

Information shown in Fig. 3 and Table 2 are used as input for the CADDIES Caflood modelling tool, coupled with extreme rainfall scenarios derived from the methodology discussed in previous section. For the analyses, two different return periods for the rainfall events are considered, namely $T_1 = 10$ yr and $T_2 = 200$ yr, consistently with the observation that urban flooding can be due to either low-frequency events causing surcharge of the underground sewer systems with consequent overflowing, or high-frequency events caused by local, unpredictable deficiencies of the drainage system (Palla et al., 2018). Urban drainage networks are usually designed for low return periods; nonetheless it is quite common to understand consequences of highly extreme rainfall events in urban areas (Kaspersen et al., 2017; Martínez-Gomariz et al., 2019; Cao et al., 2020; Li and Willems, 2020), although the statistical meaning of return periods under changing climates should be carefully considered (Cooley, 2013).

3.2. Rainfall data

Table 3 shows the members of the adopted ensemble of climate experiments, exploiting six different GCM/ESMs and eight different RCMs in nineteen different combinations. In case of experiments sharing same GCM/ESMs and RCMs (e.g. members #5 and #8 in Table 3), different configurations, for instance in terms of parametrizations and/or tuning, can result in different outputs. The local extreme rainfall regime for the case study under climate changes is provided by Equation (2), using as observational reference the local design IDF curve over the period 1971–2000, obtaining 19 IDF curves expected in the future horizon 2071–2100 for RCP 4.5 and RCP 8.5 scenarios. As previously mentioned, subsequent analyses focus on two relevant return periods ($T_1 = 10$ yr and $T_2 = 200$ yr), for a total number of $2 \times 2 \times 19 = 76$ simulations under climate change, plus two reference simulations under present climate conditions.

4. Results of the impact simulation Chain

4.1. Local extreme rainfall regime for the case study under climate change

Table 3 provides, for each of the 19 climate projections, the annual maximum 1-hr rainfall intensity obtained from Equation (2) for the two reference return periods ($T_1 = 10$ yr and $T_2 = 200$ yr) and the two considered RCP scenarios. The observed annual maximum 1-hr rainfall intensity, provided by the design IDF curve for the reference period 1971–2000, hereafter referred to as "I_0", is equal to 40.4 mm/h and 71.4 mm/h for T_1 and T_2 respectively.

Fig. 4 shows the Depth – Duration curves obtained by means of Equation (2) for different rainfall durations. As Fig. 4 (as well as Table 3 for 1-hr duration only) shows, variability of climate projections is a function of return period and concentration scenarios: for fixed RCP scenario, variability is the largest for the largest return period, whereas, for fixed T, variability is the largest under the RCP 8.5 scenario, with the effect of concentration scenario more pronounced than that of return period. Variability also shows an increasing dependence on rainfall duration. Under RCP 4.5 rainfall values appear uniformly distributed in the variability range, whereas under RCP 8.5 rainfall values gather in the lower part of the range, close to the reference IDF curve for current climate, showing a small number of significantly diverging values representing models #13, #18 and #10 from the highest to the lowest rainfall depth. In all cases, the upper and lower bounds of the variability range correspond to models #13 and #1 respectively; #1 also provides rainfall depth values lower than the observed one under RCP 4.5, for all

Table 2
Soil parameters for flood inundation modelling.

Land Use Class	Land Use Type	Roughness s*m$^{(-1/3)}$	Infiltration rate (mm·h^{-1})
A	Impervious surfaces (roads, parking lots and manmade surfaces)	0.02	27
B-1	Green areas, slope 0–4%	0.03	16
B-2	Green areas, slope 4–8%	0.03	13
B-3	Green areas, slope 8–12%	0.03	10
B-4	Green areas, slope 12–16%	0.03	6
B-5	Green areas, slope > 16%	0.03	4
C	Manmade pervious areas (sport facilities and railroads)	0.03	30

Table 3
Annual maximum 1-hr rainfall intensity (mm/h) under observed (locally available IDF curve) and future (bias-corrected) climate (maximum and minimum values in bold).

| Climate experiment	GCM	RCM	$T_1 = 10$ years		$T_2 = 200$ years	
			RCP 4.5	RCP 8.5	RCP 4.5	RCP 8.5
#1	CNRM-CM5_r1i1p1	CCLM4-8-17_v1	**39.36**	**41.72**	**69.57**	**73.74**
#2	CNRM-CM5_r1i1p1	Aladin53	41.71	50.52	73.73	89.30
#3	CNRM-CM5_r1i1p1	Alaro	42.38	49.83	74.92	88.09
#4	CNRM-CM5_r1i1p1	RCA4_v1	51.81	56.51	91.59	99.89
#5	EC-EARTH	RACMO22E_v1	45.41	46.12	80.28	81.52
#6	EC-EARTH	HIRHAM5_v1	48.89	49.98	86.43	88.35
#7	EC-EARTH	CCLM4-8-17_v1	42.41	42.78	74.97	75.63
#8	EC-EARTH	RACMO22E_v1	45.03	44.92	79.59	79.40
#9	EC-EARTH	RCA4_v1	44.36	48.82	78.41	86.31
#10	IPSL-CM5A-MR_r1i1p1	WRF331F_v1	51.42	66.60	90.90	117.73
#11	IPSL-CM5A-MR_r1i1p1	RCA4_v1	46.68	45.88	82.52	81.10
#12	HadGEM2-ES	CCLM4-8-17_v1	44.97	51.88	79.50	91.70
#13	HadGEM2-ES	RACMO22E_v1	**52.48**	**76.46**	**92.76**	**209.20**
#14	HadGEM2-ES	RCA4_v1	47.81	49.53	84.51	87.56
#15	MPI-ESM-LR_r1i1p1	CCLM4-8-17_v1	40.65	43.40	71.86	76.72
#16	MPI-ESM-LR_r1i1p1	REMO2009	48.48	47.17	85.70	83.38
#17	MPI-ESM-LR_r1i1p1	RCA4_v1	49.70	48.65	87.85	85.99
#18	MPI-ESM-LR_r1i1p1	REMO2009	50.28	56.18	88.89	129.68
#19	NorESM1-M	HIRHAM5	42.67	50.06	75.42	88.49
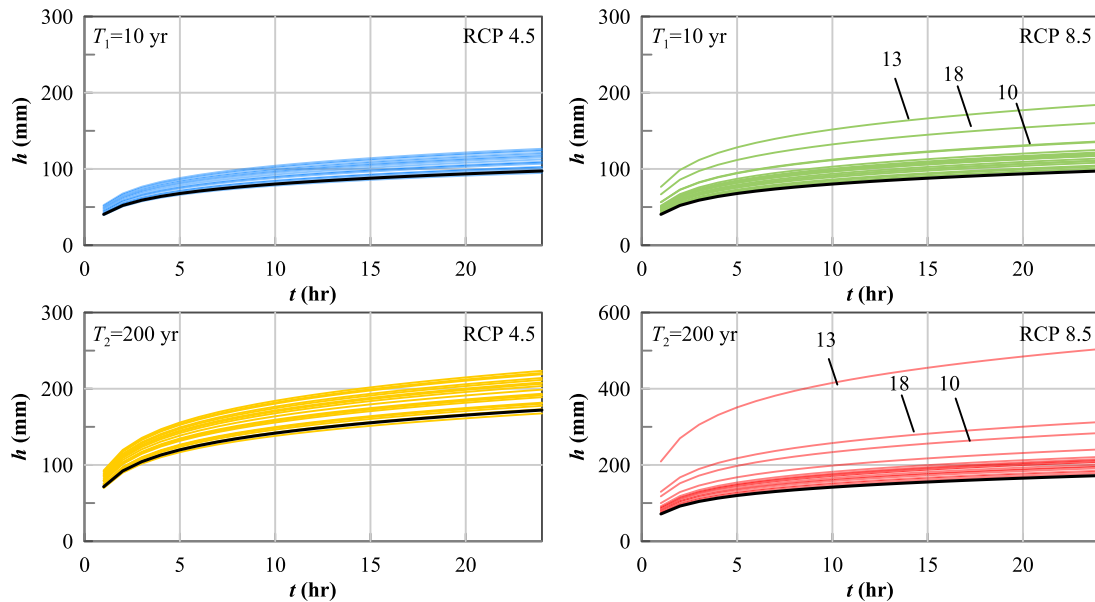
Fig. 4. Depth-Duration curves for the case study for two different return periods and two different RCP scenarios (local IDF curve used as baseline for climate change evaluation in black). DD curves expected in the future build on the methodology and application presented by Padulano et al. (2019). IDs of projections providing extremely high rainfall depths (Table 3) under RCP 8.5 are also shown.

rainfall durations.

4.2. Flood hazard evaluation

4.2.1. Statistical features of flood-related variables

Table 4 shows the main statistical features of the outcomes of the examined flood inundation models under peak conditions. For each combination return period/RCP scenario, the statistical properties are referred to the complete ensemble of simulations, including the baseline. For each variable, results are presented in terms of mean and median value, standard deviation, variability range, skewness coefficient, and variation coefficient. As Table 4 shows, the water depth variable D exhibits a significantly skewed frequency, closely followed by total head H and, secondly, by unit discharge U, whereas flow velocity V only shows a limited, although non-negligible, skewness coefficient. Consistently, D and H show very small central values compared to the upper limit of the

variability range, and mean values roughly double than the 50th percentile. Mean, median (although to a lower extent), maximum value and standard deviation uniformly increase moving from T_1/RCP 4.5 to T_2/RCP 8.5; conversely, skewness shows an increasing behaviour for V but a decreasing behaviour for D, and the opposite occurs for the coefficient of variation. Similar considerations for combined variables U and H suggest that the frequency distribution of total head is mostly affected by water depth D, whereas distribution of U also accounts for the statistical features of variable V.

4.2.2. Cumulative hazard indicators

Fig. 5 shows RVI_p and FAI_p values for all the simulated scenarios. For each return period ($T_1 = 10$ years in green, $T_2 = 200$ years in red) RCP 4.5 and 8.5 scenarios are identified by cross markers and triangle markers, respectively. However, due to the distribution of simulated rainfall intensities, most data points gather close to the respective

Table 4
Statistical properties of CADDIES Caflood simulations (peak conditions).

Variable	Scenario	mean × 10	median × 10	min × 10	max	σ × 10 [a]	γ [b]	CV [c]
D (m)	T_1, RCP 4.5	0.46	0.23	0.10	3.30	0.84	9.17	1.81
	T_1, RCP 8.5	0.48	0.23	0.10	3.32	0.89	9.03	1.87
	T_2, RCP 4.5	0.53	0.23	0.10	3.33	1.13	8.58	2.12
	T_2, RCP 8.5	0.55	0.23	0.10	4.11	1.21	8.88	2.21
V (m/s)	T_1, RCP 4.5	1.97	1.60	0.00	1.53	1.55	1.76	0.79
	T_1, RCP 8.5	2.06	1.68	0.00	1.75	1.60	1.76	0.78
	T_2, RCP 4.5	2.50	2.01	0.00	1.88	1.82	1.75	0.73
	T_2, RCP 8.5	2.63	2.10	0.00	2.38	1.90	1.79	0.72
U (m²/s)	T_1, RCP 4.5	0.07	0.03	0.00	0.26	0.11	5.10	1.61
	T_1, RCP 8.5	0.07	0.03	0.00	0.39	0.12	5.21	1.62
	T_2, RCP 4.5	0.11	0.04	0.00	0.48	0.17	5.05	1.62
	T_2, RCP 8.5	0.12	0.05	0.00	1.12	0.20	6.01	1.70
H (m)	T_1, RCP 4.5	0.49	0.26	0.08	3.30	0.83	9.12	1.70
	T_1, RCP 8.5	0.51	0.27	0.05	3.32	0.89	8.97	1.75
	T_2, RCP 4.5	0.58	0.28	0.03	3.33	1.13	8.48	1.95
	T_2, RCP 8.5	0.60	0.28	0.09	4.11	1.21	8.74	2.03

[a] Standard deviation.
[b] Coefficient of variation (nondimensional).
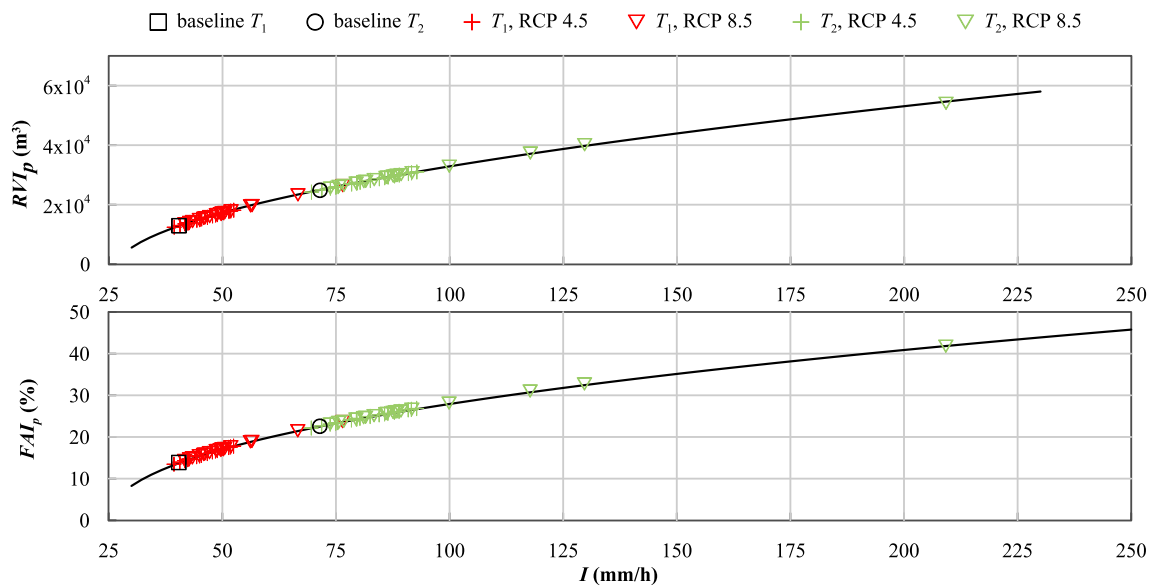[c] Skewness coefficient (nondimensional).

Fig. 5. Lumped indicators RVI_p and FAI_p for cumulative hazard as a function of rainfall intensity as provided by CADDIES Caflood. Regression curves in black ($R^2 > 98\%$ in both panels); different colours identify different return periods; different markers identify baseline, RCP 4.5 and RCP 8.5 scenarios.

baseline value, represented by black markers (which is also the minimum simulated rainfall value for RCP 8.5, and the second minimum value for RCP 4.5), with only a limited number of particularly high values, representing climate projections #13, #18 and #10 under RCP 8.5.

For both metrics, data points perfectly align along a regression curve (with coefficient of determination $R^2 > 98\%$ for both indicators), showing an increasing dependence of both runoff volume and flooded area on rainfall intensity; FAI_p values show that, for the most critical rainfall scenario, the study area is only flooded at about 40% with $D \geq 1$ cm. The structure of the dependence is power-like in both cases, with RVI_p and FAI_p gradually increasing with I with a power of about 0.5 in both cases; for about $I > 60$ mm/h the last part of both curves can be considered linear.

4.2.3. Operational hazard models

Fig. 6 shows, for each return period, the amount of pilot area subject to hazard indicators D, U and H classified according to the criteria identified in Table 1, as a function of rainfall intensity I. For each hazard

model, hazard classes are labelled from 1, which identifies the lowest hazard level, to 3 (highest hazard for the 3-class repartition criterium) or 5 (highest hazard for the 6-class repartition criterium, where the sixth hazard class in Table 1 was never attained). Consistently with Table 3 and Fig. 5, moving from the lowest to the highest rainfall intensity in each panel of Fig. 6 corresponds to moving from RCP 4.5 to RCP 8.5. Moving from left panel to right panel for each row of Fig. 6 corresponds to moving from T_1 to T_2, with data points gathering along the same curve (partitioned in two panels to improve visual inspection) for each hazard class, similarly to RVI_p and FAI_p in Fig. 5. The wide overlap between the two concentration scenarios for each of the investigated return periods makes the visual discrimination between RCP 4.5 and RCP 8.5 hardly possible. In all the panels of Fig. 6, the baseline values are also shown as black markers, pointing to the hazardous area values AWC under present climate conditions for both return periods.

In all the examined scenarios, the widest portion of the pilot area is subject to the lowest hazard, with AWC values always higher than 10%, whereas the hazardous surface decreases with increasing hazard level. For all the hazard models the dependence of AWC on rainfall intensity is
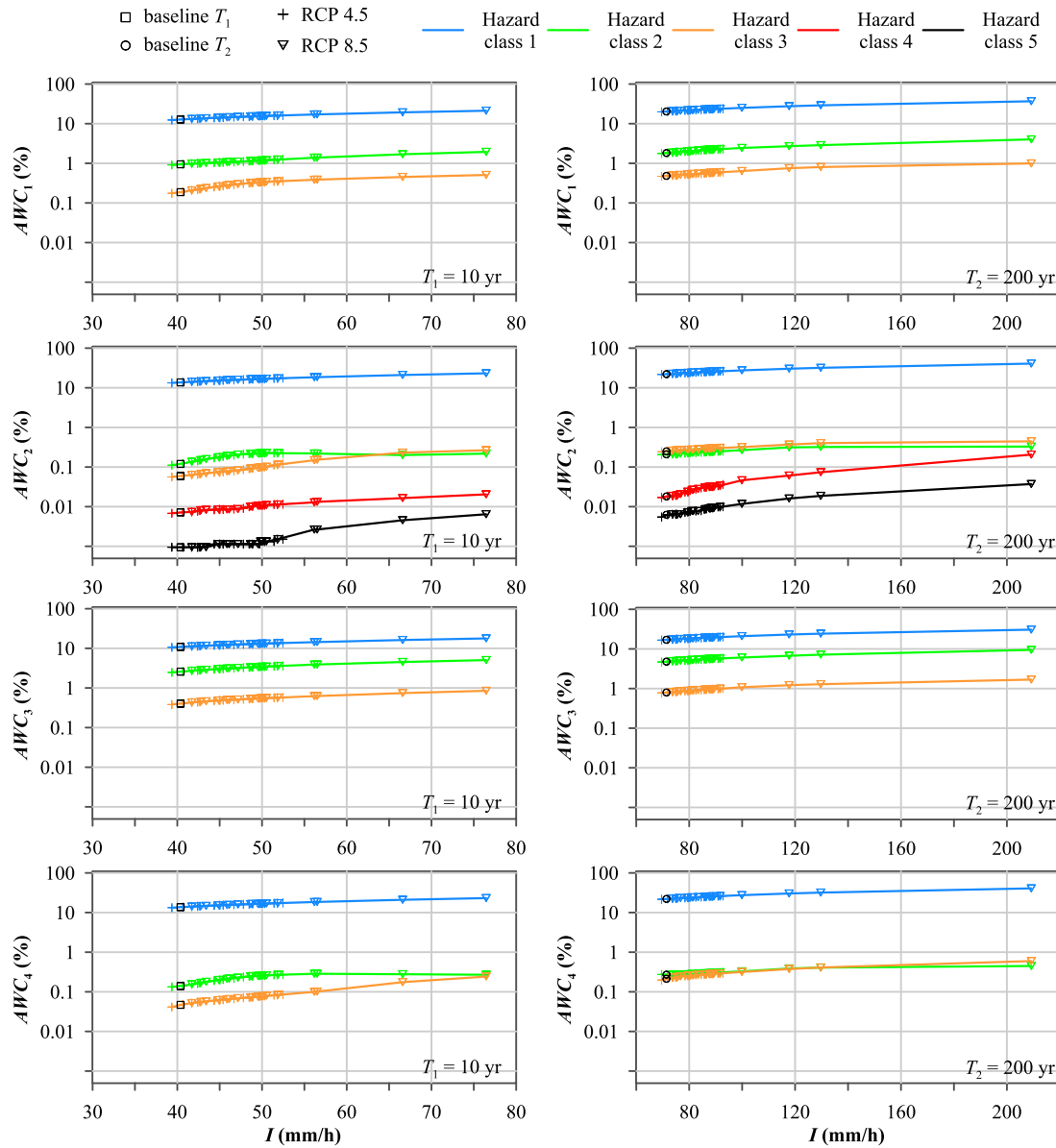
Fig. 6. Results of hazard models in Table 1 for 19 climate models under RCP 4.5 and RCP 8.5 for $T_1 = 10$ years (left column) and $T_2 = 200$ years (right column), expressed in terms of rainfall intensity (mm/h) and Area Within the Class (% of inundable area). Moving from the lowest to the highest I in each graph corresponds to moving from RCP 4.5 to RCP 8.5. Moving from left to right for each row corresponds to moving from T_1 to T_2, with data points gathering along the same curve for each hazard class, partitioned in two columns to improve visual inspection. Different colours identify different hazard classes; different markers identify baseline, RCP 4.5 and RCP 8.5 scenarios.

a function of the hazard class. Specifically, all hazard classifications show a lowest class (H1), corresponding to a low hazard condition (where all the indicator values are lower than the minimum threshold) with an almost constant *AWC* value which is also the maximum among the classes, implying that most of the pilot area (with a percentage always higher than 10%) is subject to the lowest hazard due to inundation despite experiencing a water depth ≥ 1 cm. For increasing hazard level, the hazardous area decreases, on average, and the dependence on rainfall increases. For the highest hazard classes (see for example AWC_2) the amount of exposed pilot area attains very small values (lower than 0.1%) but the dependence on rainfall intensity is significant in the entire range of investigated rainfall scenarios.

The different hazard classifications show a relevant similarity especially in the estimation of the area exposed to a low hazard (H1). The classifications based on water depth D (hazard models #1 and #3) show a direct consistency with the statistical properties of water depth shown

in Table 4, so that the lower is the threshold, the higher is the area characterized by a water depth lower or equal to the threshold. For instance, the amount of wet area exposed to $D < 10$ cm (H1 for hazard model #1) is larger than that exposed to $D < 5$ cm (H1 for hazard model #3), and the amount of wet area exposed to $D \geq 30$ cm (H3 for hazard model #1) is smaller than that exposed to $D \geq 20$ cm (H3 for hazard model #3).

The classifications based on derived variables (hazard models #2 and #4) show a different behaviour compared to the D-based classifications especially in the estimation of higher hazard classes, presumably due to the effect of the velocity parameter. Specifically, the *AWC* curves for H2 and H3 classes swap their position for the highest rainfall intensities under T_1 for hazard model #2, and for both return periods for hazard model #4. This happens because, whereas *AWC* values for H3 constantly increase with increasing I, *AWC* values for H2 increase at first with I, and then they decrease (or reach a plateau) with increasing I for

about $I > 50$ mm/h for T_1, and for about $I > 120$ mm/h for T_2. This behaviour should not be considered anomalous, since both quantities H and U build on two variables D and V which are often opponent: in each cell of the domain there usually are either high depths and low velocities, or low depths and high velocities, and the trend of their summation or product cannot be predicted a priori because it is very site-specific. For hazard model #2, in the range of T_2, the amount of pilot area exposed to H3 hazard is larger than that exposed to H2 hazard for every simulated rainfall intensity. Finally, comparison of H1, H2 and H3 values between hazard models #2 and #4 shows that the two criteria are substantially coincident.

4.3. Analysis of normalized indicators

As shown in the results section, the raw outcomes of flood inundation modelling (D, V and related variables) strictly depend on the rainfall intensity value used as input. This is particularly evident in Fig. 5 for cumulative hazard metrics, where the increase in rainfall intensity with respect to the baseline conditions is found to be the only predictor of the increase in peak runoff volumes and flooded areas.

However, the present research is particularly oriented to understand if, and to what extent, flood hazard is affected by changes in climate conditions, and this depends not only on the rainfall input, but also on the hazard model adopted. As shown by Figs. 6 and 7, for example, the amount of area affected by any assigned level of flooding proves to be diversely affected by any increase in rainfall values compared to the baseline conditions; in other words, increases in rainfall values as those provided by climate change under the same return period provide different increase in the affected areas. With this aim, this section provides an analysis of normalized indicators: in other words, results shown in Figs. 5–7 are rearranged so that each metric x is represented by its normalized value $x' = x/x_0$, where x_0 corresponds to baseline conditions.

4.3.1. Normalized cumulative hazard indicators

Fig. 7 shows normalized peak indicators $RVI'_p = RVI_p/RVI_{p,0}$ and $FAI'_p = FAI_p/FAI_{p,0}$ as a function of normalized rainfall intensity $I' = I/I_0$ for all the exploited scenarios, which were dimensionally represented in Fig. 5. For fixed return periods, moving from RCP 4.5 to RCP 8.5 implies increasing rainfall intensity values (Table 3), so that data points continuously develop along a line from the smallest to the largest

abscissa. However, two different lines occur for the two investigated return periods, due to the different reference conditions. In the range of investigation the behaviour can be effectively considered linear, with a coefficient of determination R^2 higher than 98% in all cases.

For fixed return period, Fig. 7 shows that the transformation of rainfall into runoff can be represented by a linear relation between the considered normalized variables. The equations for the regression lines, shown in each panel, are such that a unitary increase in rainfall does not imply a unitary change in flooding conditions, in terms of either runoff volume or flooded area. This confirms the recognized non-linearity of the rainfall – runoff transformation (Todini, 1988), which is represented in Fig. 7 by means of the 1:1 line. The functional form of the regression lines, as well as the parameters' values, depend on the overall features of the case study judged relevant for the rainfall – runoff transformation. Neglected or simplified processes, such as the role of infiltration and the effect of the drainage network, may alter observed linearity. Among the experienced return periods, regression lines of T_2 data points show a lower slope, implying that the more critical is the baseline scenario, the lower can be the increase in criticality due to an increase in rainfall with respect to baseline. This is particularly obvious for FAI'_p, since flooded area cannot overcome 100%. Although only two return periods are examined in the research, it is expected that the slope of the regression line decreases with increasing return period.

The aspect and location of the regression line could be altered by modifying drainage characteristics, for instance including adaptation measures; in this perspective, the diagram proposed in Fig. 8 could act as an abacus, driving the selection of interventions and providing information about the feasibility and effectiveness of selected actions. For example, one or multiple interventions could be simulated with the desired effect of decreasing the slope of the regression line compared to the reference condition (e.g. that referring to present climate and drainage settings), so that extreme events would cause lower flood levels. It is worth noting that, as Fig. 7 shows, normalized flooded area increases to a lower extent than runoff volume with increasing normalized rainfall intensity. In other words, when using diagrams such as the one proposed in Fig. 7 for viability analysis of adaptation measures, the same performance in terms of slope reduction cannot be ensured for both indicators at the same time.
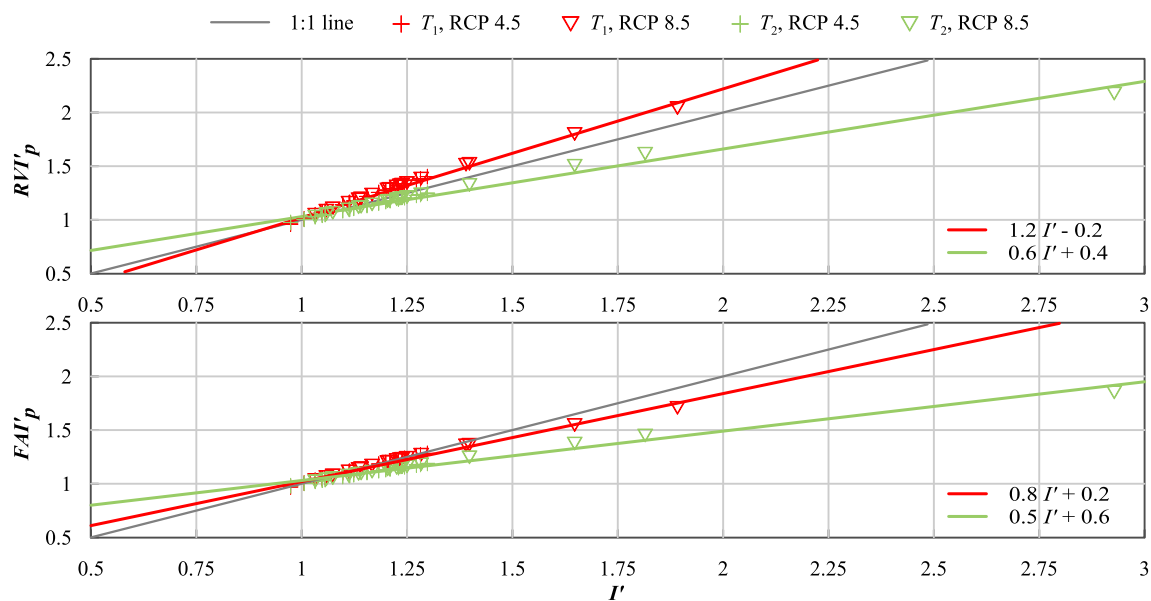

Fig. 7. Normalized lumped indicators RVI'_p and FAI'_p as a function of normalized rainfall intensity I' (1:1 line in grey, regression lines in red for T_1, in green for T_2). $R^2 > 98\%$ in both panels and for both return periods. (For interpretation of the references to colour in this figure legend, the reader is referred to the web version of this article.)
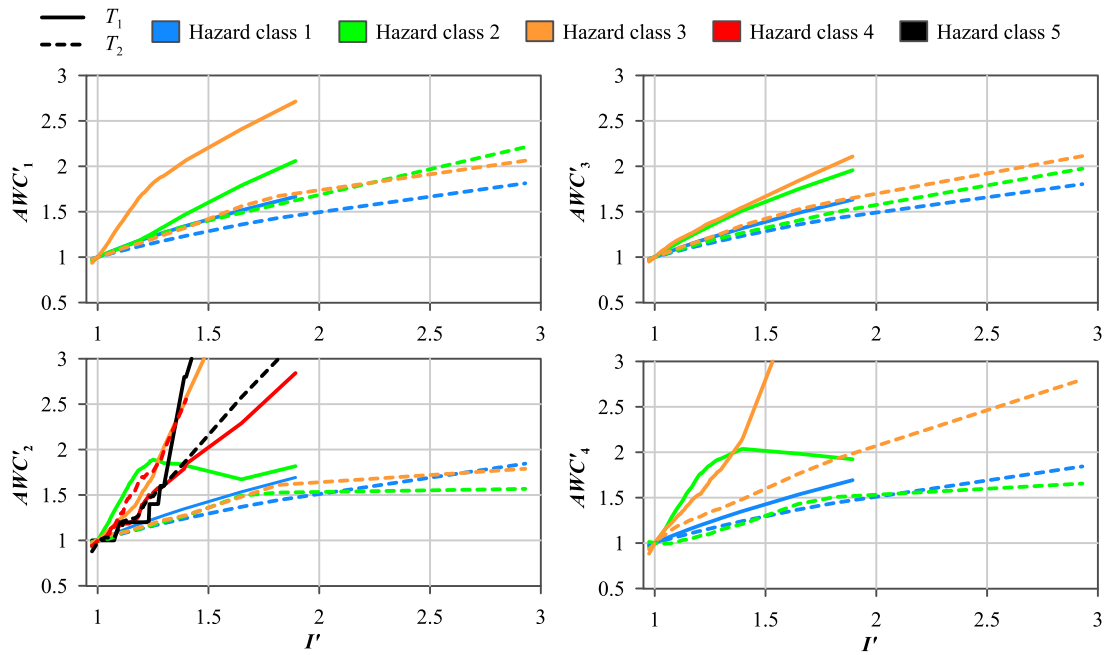
Fig. 8. Normalized results of operational hazard models in Table 1 for 19 climate models under RCP 4.5 and RCP 8.5 for T_1 (solid lines) and T_2 (dotted lines). Hazard classes are identified in colours grading from blue (minimum hazard level among all hazard models) to black (maximum hazard level among all hazard models). (For interpretation of the references to colour in this figure legend, the reader is referred to the web version of this article.)

4.3.2. Normalized operational hazard model results

Fig. 8 shows the same results shown in Fig. 6 but provides, on the vertical axis, normalized values AWC', namely the ratio of AWC to the baseline value AWC_0, whereas normalized intensity values are used for the horizontal axis. For each hazard model and each hazard class, two curves are provided corresponding to T_1 (solid line) and T_2 (dashed line); for each curve, increasing I' implies moving from RCP 4.5 to RCP 8.5 scenario. In all cases, for fixed I', AWC' is always higher for the smaller return period; this is expected since T_1 is characterized by smaller intensity values than T_2, corresponding to the lower branches of all curves in left panels of Fig. 6, where the change in AWC with I is still non-negligible compared to the flat curves in right panels of Fig. 6.

For hazard models #1 and #3, for assigned normalized intensity and return period, normalized AWC increases with increasing hazard level. In other words, any increase in rainfall intensity causes an increase in the extent of exposed areas which is more significant for the highest hazard levels. The behaviour is quite similar between models #1 and #3 with the evident exception of H3 class for T_1 scenarios, where hazard model #1 provides a significantly larger inflation of exposed areas. For instance, for the T_1 scenario, inflating rainfall intensity by 1.5 (in other words, increasing baseline intensity by 50%) implies inflating areas exposed to H3 by 2.2 according to hazard model #1, by 1.7 according to hazard model #3.

The classifications based on derived variables (hazard models #2 and #4) roughly confirm the above-mentioned results. Consistently with Fig. 6, H2 and H3 show an opposite trend in the range of T_1 intensity values, with the H3 curve monotonically increasing, and the H2 increasing (but less than H3) and then slightly decreasing with increasing intensity, which reflects in the elbow shown in Fig. 8 for both hazard models. For hazard model #2, H4 and H5 curves in Fig. 8 show a very rapid increase in exposed areas with normalized intensity (for instance, more than triplicating with doubling rainfall intensity) although with some erratic behaviours, especially for the smaller I' values, probably due to the fact that AWC_2 values for those classes are very small (Fig. 6) and possibly affected by estimation errors and approximations.

4.4. Flood hazard mapping

Fig. 9 shows the hazard maps provided by CADDIES Caflood for the most critical rainfall scenario, characterized by a return period $T_2 = 200$ years under the RCP 8.5 concentration scenario for the climate projection #13, corresponding to a rainfall intensity $I = 209$ mm/h. In Fig. 9 only three flood hazard classifications are represented, namely the classification based on unit discharge U (hazard model #2), the classification based on water depth D (hazard model #3) and the classification based on total head H (hazard model #4); hazard model #1 can be considered redundant. As already mentioned in previous sections, lacking flood observations in the case study for validation purposes, hazard maps in Fig. 9 should be only analysed in comparison among different rainfall scenarios. However, a fair significance of results can be assessed considering that the inundation model correctly captures critical spots such as the underpass, the areas adjacent to the football stadium and the entrance of the railway station. Hazard model #2 particularly emphasizes critical conditions at the entrance of the underpass, whereas hazard model #3 provides a non-negligible high hazard level for the main railroad. Results of hazard model #4 can be considered similar to #2, but with the highest hazard levels condensed in a unique class.

The outcomes of flood hazard mapping show that for the case study the adopted criteria are poorly selective, implying that most of the pilot area comes under the lowest hazard class, whereas a very small portion of the domain is assigned to the highest hazard levels. This is consistent with the statistical properties reported in Table 4 compared to the threshold values for hazard models in Table 1, with median values for all variables not far from the lowest thresholds, coupled to a deeply skewed distribution.

4.5. Mapping the propagation of climate projections' variability

Fig. 10 shows, for each return period and each concentration scenario, and for each climate simulation chain, the path of normalized variables representative of all the steps of the modelling chain:
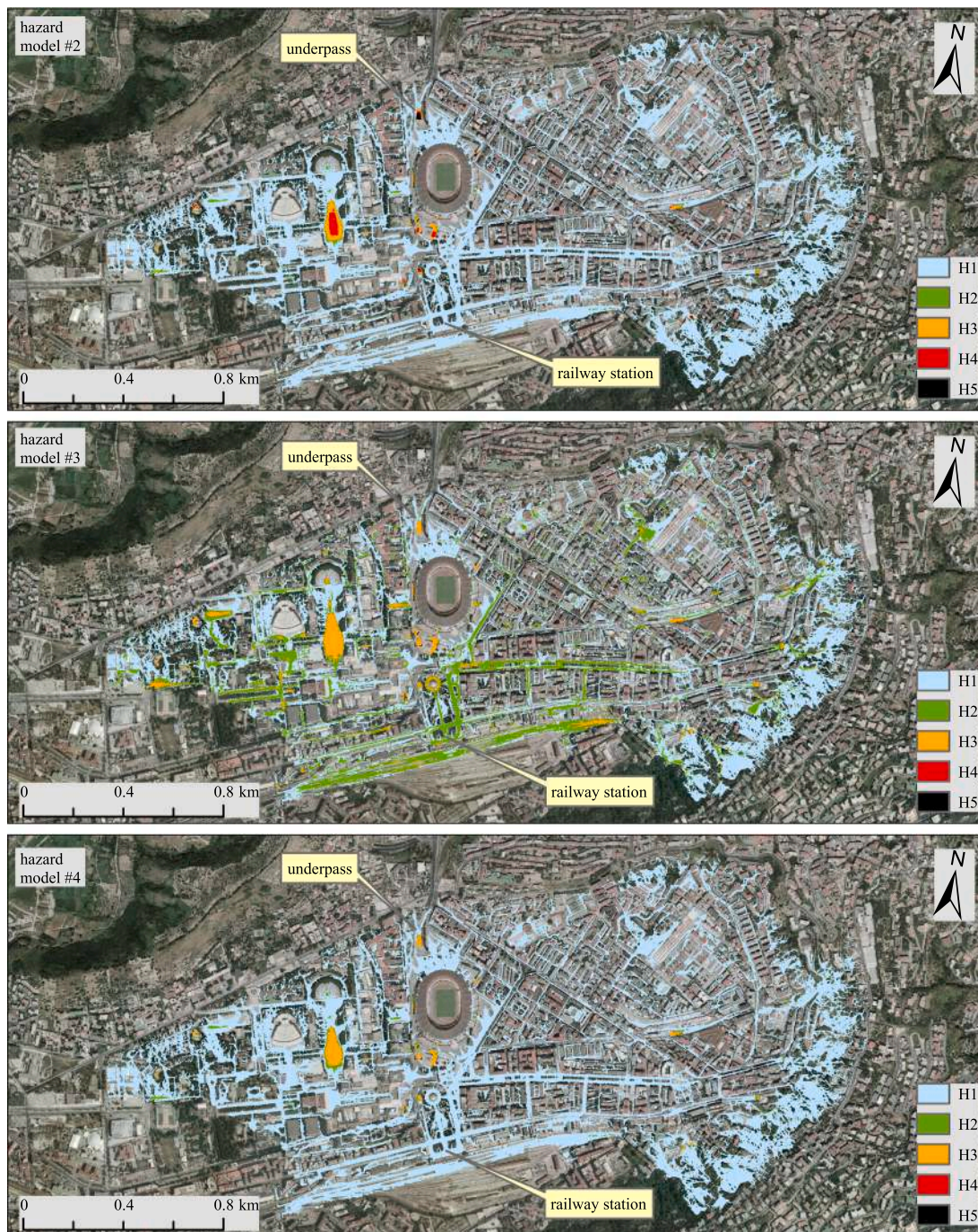
Fig. 9. Hazard maps for T_2/RCP 8.5 scenario for climate projection #13: hazard model #2 based on unit discharge U, hazard model #3 based on water depth D, hazard model #4 based on total head H. H4 and H5 classes are only possible for hazard model #2.

(i) the climate change module: it accounts for projection uncertainties (e.g. IPCC socio-economic and greenhouse gas concentration scenarios, climate model assumptions, parametrizations, discretization) as well as bias correction. It is represented in Fig. 10 by normalized annual maximum 1-hr rainfall intensity I.

(ii) the flood inundation module: it accounts for the uncertainties proper of the rainfall-runoff transformation modelling (assumptions, parametrizations, discretization) along with previous variabilities. Among the investigated variables, normalized mean μ and standard deviation σ of water depth D and flow velocity V occurring over the pilot area are considered in Fig. 10.

(iii) the cumulative hazard modelling: in Fig. 10, normalized FAI'_p and RVI'_p are chosen. These indicators can be considered representative of the inundation modelling as well, since they only depend on water depth D.

(iv) the operational hazard modelling: it accounts for the arbitrariness in the definition of threshold values for hazard classification along with previous variabilities. Normalized AWC' is chosen as representative, with AWC values computed for the lowest hazard class for each hazard model in Table 1 (shortened as H1′ in Fig. 10). H1 class was preferred since it is the most represented hazard level for all hazard models.
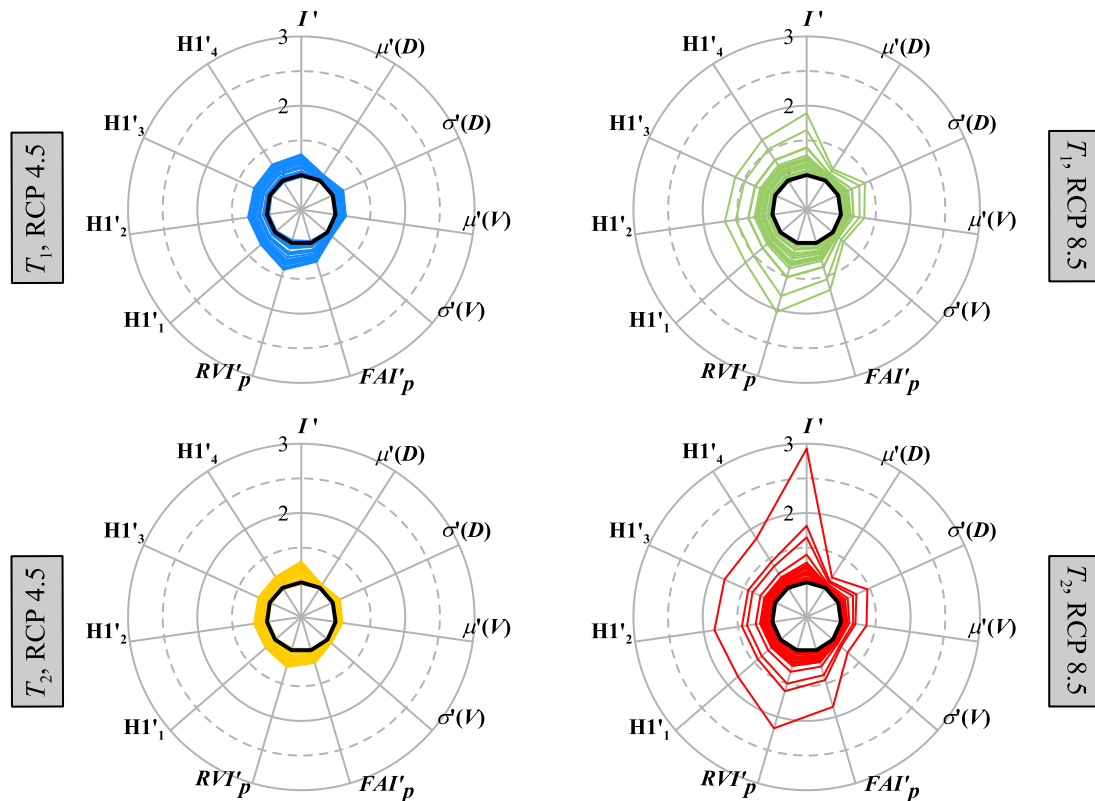
Fig. 10. Propagation of variability in climate projections through the impact modelling system for all simulated scenarios. Each line maps a single simulation starting from rainfall intensity (vertical axis), moving clockwise through raw flood features and ending to hazard model results. All variables are normalized by their corresponding baseline values. Baseline simulations are shown as black circles with unitary values for all normalized variables.

The radar graph in Fig. 10 was considered the most effective tool to visually map and inspect results, since it is acknowledged as particularly suitable to show multivariate data. Each of the normalized indicators identified in (i)-(iv) is assigned an axis, with a common origin at the center of the graph. Each line maps the main outcomes of each single flood simulation, starting from rainfall intensity (vertical axis I' and entry point for the radar graph lines), moving clockwise through raw flood features (axes from $\mu'(D)$ to $\sigma'(V)$) and cumulative hazard features (axes FAI'_p and RVI'_p) and ending at the operational hazard features (axis from $H1'_1$ to $H1'_4$).

Fig. 10 shows that the spread in rainfall values used as input, which is due to the use of an ensemble of climate experiments (Table 3), slightly reduces moving from climate change modelling to flood modelling, implying a dampening effect of the flood modelling for all scenarios. In other words, a given increase in rainfall intensity with respect to present climate causes a lower increase in water depth features (particularly in the mean values) and in flow velocity features (particularly in the standard deviation). In turn, moving towards hazard modelling causes variability to inflate with respect to flood modelling, but keeping within a similar level with respect to rainfall variability. Among all the hazard metrics, variability in RVI'_p proves to be the most inflated. Results of the four tested hazard models can be considered coincident; variability in $H1'$, along with variability in FAI'_p, attains values similar to variability in rainfall. This is especially true for the RCP 4.5 scenarios which exhibit the lowest variability in rainfall increase with respect to the baseline, with I' always lower than 1.5. Instead, for the RCP 8.5 scenarios, showing larger rainfall variability (with maximum I' almost equal to 2 and 3 for T_1 and T_2 respectively), a dampening effect of the hazard modelling can be appreciated in addition to the mitigating effect of the rainfall – runoff transformation.

The behaviour of single climate simulation chains is consistent throughout the process, implying that the climate projections providing

the highest increase in rainfall intensity also provide the highest increase in all the other metrics. This is particularly visible for T_2 under RCP 8.5, where lines representing single climate experiments are concentric and never intersect. Finally, as also shown in Fig. 7 and Fig. 8, for both RCP scenarios variability in normalized metrics is narrower for T_2 than for T_1, implying that "alterations" due to the effect of climate change are not evenly distributed for all magnitudes of rainfall events (the hazard source), so that more significant changes with respect to present climate should be expected for the less critical events.

As a final comment, Fig. 10 shows that the total spread in all the considered normalized variables keeps within the circle corresponding to the maximum experienced I', which is roughly equal to 1.3 for T_1/RCP 4.5 (corresponding to an increase in rainfall intensity of 30% with respect to baseline), 2 for T_1/RCP 8.5 (corresponding to an increase of 100%), 1.3 for T_2/RCP 4.5 (corresponding to an increase of 30%) and 3 for T_2/RCP 8.5 (corresponding to an increase of 200%), the only exception being RVI'_p under RCP 4.5 scenarios. Within those circles, normalized statistical properties exhibit a significantly narrower variability range for all the simulated scenarios.

5. Discussion

5.1. Limitations of the work and future developments

The choice of the flood modelling tool and related parametrizations, including simplified infiltration process and sewer system conveyance, may have an influence on the outcomes of the research that could constitute promising ground for further research, comparing, for instance, the adopted flood model both to more complex tools, explicitly accounting e.g. for the presence of a sewer system, and to expeditious models usually only accounting for the elevation layout. Due to the lack of flood observations, which is a very common situation in practical

applications although usually accepted for scenario analyses, as discussed in the Introduction, it was not possible to validate the accuracy of results for any rainfall event, but it was only possible to check consistency of results basing on visual inspection of flood maps and expert judgment.

The observed skewness in flood depths, resulting from the flood inundation model, causes the extent of hazardous areas to significantly reduce with increasing hazard level, resulting in very small areas exposed to the highest hazard under future as well as present climate. Although an asymmetric distribution, skewed towards small depths, should be generally expected, the flat layout of the domain could deeply affect flood features because the distribution of water depths is significantly uniform, with a limited number of outlying locations corresponding to specific elements of the built environment (such as the underpass).

Furthermore, questions arise about the representativeness of the adopted hazard models. For the pilot area, most of the highly hazardous areas were expected, such as the underpass; however, tangible experience of the site suggests that perceived hazard is higher even for rainfall events with lower frequency. In addition, some hazard models, such as AIDR (2017), fail to capture non-negligible risks that are captured by others. This could be explained noting that flood hazard models are often conceived for fluvial flooding, with usually larger water depths and velocities and considerable damages to the exposed assets, with highly critical consequences on their structural integrity (e.g. closed streets or transport service). Instead, purely pluvial flooding conditions may affect exposed assets especially at the operational level (e.g. traffic jams, delays), and this may not be efficiently captured by those hazard models.

In any case, propagation of variability due to the adoption of an ensemble of climate projections throughout the Impact Simulation Chain was mapped using variables that were normalized by means of the corresponding baseline values referring to present climate. This reasonably ensures that results shown in Fig. 10, as well as the overall methodology, can be considered valuable despite the simplifications and possible inaccuracies caused by the flood inundation model (governing equations, numerical scheme, parametrizations for simplified processes) as well as by the particular choice of hazard metrics.

5.2. Potential impacts on the related literature

Despite the limitations highlighted in the previous section, the main findings of this research may have several impacts on the related literature, with specific reference to the estimation of climate change impacts on flooding and the use of flood modelling tool.

This paper proposes a multi-purpose impact analysis, based on cumulative and operational hazards indicators. In this sense, the work offers novel points of view for those lines of research involved in the development of flood indices to identify spatial patterns of flood risk within a given studied areas (Xu et al., 2019; Shadmehri Toosi et al., 2020). Moreover, some of the indicators considered here, such as *RVI* and *FAI*, can be considered similar to other synthetic parameters analyzed in the literature (see for example Löschner et al., 2017; Zhou et al., 2019) confirming their value when dealing with urban flood hazard assessment in a climate change context.

The outcomes of the research can be of aid to water infrastructure managers, designers and policy makers when dealing with the impacts of climate change in flood-prone urban areas, and its relationship with the effects of increasing urbanization (Mahmoud and Gan, 2018). Furthermore, the impact simulation chain proposed in this paper can be further used for other purposes such as the quantification of benefits related to climate change adaption measures, which have been devoted particular attention in the recent literature (see, for example, Zhou et al., 2018; Ghodsi et al, 2020).

It is also important to underline the potential impact of this research for urban flood modelers, with particular reference to the application of

CADDIES Caflood model. This numerical code was extensively applied for classic flood propagation situations (Guidolin et al., 2016) and only recently it has been also used for rain-on-grid simulation (Wang et al., 2018) where the rainfall input is directly considered within the hydrodynamic model. It should be recalled that these simulations are very challenging from a numerical point of view (Cea and Bladé, 2015) and, due to the increasing use in the literature for both basin-scale (i.e. Ferraro et al., 2020) and urban scale (i.e. Guo et al., 2021) applications, further evidence is required about the suitability of the software package for pluvial flooding (Costabile et al., 2020b).

As finally concerns the climate change perspective, in the field of urban flooding the paper presents a unique example of propagating the spread in rainfall coming from a large ensemble of climate projections throughout a comprehensive modelling chain, from the quantification of local effects of climate change up to flood hazard evaluations. The main difference with similar outcomes, such as those shown by Kaspersen et al. (2017), lies in the decision of mapping the results of each flood simulation (taking as input a specific rainfall value) separately. This approach stems from the assumption that each different climate projection provides an equiprobable future rainfall scenario, rejecting the common idea that particularly high future extreme rainfall values are outliers and, consequently, less credible than the moderate ones.

6. Conclusions and lessons learnt

A complete Impact Simulation Chain was performed consisting of a climate change modelling module, an urban flood modelling module and a flood hazard modelling module. Analyses were performed for two different return periods ($T_1 = 10$ years and $T_2 = 200$ years) for the test case of Fuorigrotta, City of Naples (Italy).

The paper fills the current gap in the analysis of climate change impacts on urban flooding by relying on a full ensemble of climate projections (reflecting the use of a large ensemble of climate experiments derived from different GCMs/ESMs coupled with different RCMs under different RCP scenarios), where single members were considered equiprobable, in opposition to current impact literature usually targeting ensemble mean and standard deviation or relevant percentiles. The main goal of the research consisted in understanding how the variability in the rainfall input propagated within the system and reflected onto the urban environment and related sub-systems. Despite the abovementioned limitations, the following conclusions can be drawn:

- variability of climate projections is a function of return period and concentration scenarios: for fixed RCP, variability is the largest for the largest return period, whereas for fixed *T* variability is the largest under RCP 8.5, with the effect of concentration scenario more pronounced than that of return period.
- Raw output variables of flood inundation model exhibit a considerably asymmetrical distribution, with very large skewness coefficients for water depth, closely followed by total head and unit discharge, and smaller skewness values for flow velocity.
- Analysis of cumulative hazard indicators shows that runoff volumes and flooded areas increase with increasing rainfall with a power of about 0.5. This implies that, with respect to current climate, for a fixed increase in rainfall the increase in both flood indicators has a magnitude which decreases with increasing return period. For the lower return period, the increase in runoff volumes is roughly equal to the increase in rainfall, whereas it is smaller for the higher return period. The experienced increase in flooded areas is always smaller than the increase in rainfall, probably due to the elevation features of the pilot area. Although this testifies the nonlinearity of the rainfall – runoff transformation, the relationship between rainfall increase and flood features increase was found to be linear for all return periods.
- Analysis of operational hazard indicators show that, for increasing hazard level, the extent of hazardous areas decreases and the dependence on rainfall becomes more marked. For fixed hazard

level, hazardous areas are closely related to rainfall only for small intensities (namely, 10-yr return period under RCP 4.5) and then stabilize. With respect to current climate, for fixed return period the extent of hazardous areas increases more rapidly with increasing rainfall for higher than for lower hazard levels. For fixed hazard, inflation of hazardous areas is more evident for 10-yr than for 200-yr rainfall scenarios.

- Mapping the propagation of rainfall variability through the Impact Simulation Chain in terms of normalized indicators shows that the spread in normalized rainfall input envelopes the variability range of all subsequent modelling steps, including raw flood modelling outputs, cumulative and operational hazard indicators. The envelope spread is roughly equal to 1.3 for T_1/RCP 4.5 (corresponding to an increase in rainfall intensity of 30% with respect to current climate), 2 for T_1/RCP 8.5 (increase of 100%), 1.3 for T_2/RCP 4.5 (increase of 30%) and 3 for T_2/RCP 8.5 (increase of 200%). On one hand, this confirms that the higher the return period the lower the increase in flood indicators, in comparison. On the other hand, this demonstrates that concentration scenarios play a predominant role in the allocation of variability in the input and, as a consequence, in the output, with e.g. T_1/RCP 8.5 scenario providing a higher increase in flood criticality than T_2/RCP 4.5.

In terms of input data, computational effort and reliability and versatility of the outputs, the adopted inundation model provides a balance between expeditious tools, often relying on elevation only, and comprehensive hydrodynamic models, usually fed by a large amount of detailed input data. This makes the Impact Simulation Chain particularly suitable to be used for scenario analysis under climate change. The research provides a methodological framework that can be tailored to meet specific requirements and needs, adopting, for instance, different GCMs/RCMs couplings or bias-adjustment techniques, different flood models, or different hazard indicators. As a future perspective, this framework can be used to explore different uncertainty sources within the Impact Simulation Chain, as well as the feasibility and effectiveness of adaptation measures to reduce flood risks.

CRediT authorship contribution statement

Roberta Padulano: Conceptualization, Methodology, Formal analysis, Data curation, Writing - original draft, Visualization. **Guido Rianna:** Conceptualization, Methodology, Writing - review & editing. **Pierfranco Costabile:** Conceptualization, Methodology, Formal analysis, Writing - review & editing. **Carmelina Costanzo:** Conceptualization, Methodology, Formal analysis, Data curation. **Giuseppe Del Giudice:** Conceptualization, Methodology, Writing - review & editing, Supervision. **Paola Mercogliano:** Conceptualization, Writing - review & editing, Supervision.

Declaration of Competing Interest

The authors declare that they have no known competing financial interests or personal relationships that could have appeared to influence the work reported in this paper.

Acknowledgements

References

AIDR, 2017. Flood Hazard. Australian Disaster Resilience Handbook Collection. Guideline 7–3. Second Edition.

Alves, A., Vojinovic, Z., Kapelan, Z., Sanchez, A., Gersonius, B., 2020. Exploring trade-offs among the multiple benefits of green-blue-grey infrastructure for urban flood mitigation. Sci. Total Environ. 703, 134980 https://doi.org/10.1016/j.scitotenv.2019.134980.

Arnbjerg-Nielsen, K., Willems, P., Olsson, J., Beecham, S., Pathirana, A., Bülow Gregersen, I., Madsen, H., Nguyen, V.T.V., 2013. Impacts of climate change on rainfall extremes and urban drainage systems: a review. Water Sci. Technol. 68 (1), 16–28. https://doi.org/10.2166/wst.2013.251.

Arrighi, C., Pregnolato, M., Dawson, R.J., Castelli, F., 2019. Preparedness against mobility disruption by floods. Sci. Total Environ. 654, 1010–1022. https://doi.org/10.1016/j.scitotenv.2018.11.191.

Ashley, R.M., Balmforth, D.J., Saul, A.J., Blanksby, J.D., 2005. Flooding in the future - predicting climate change, risks and responses in urban areas. Water Sci. Technol. 52 (5), 265–273. https://doi.org/10.2166/wst.2005.0142.

Ban, N., Caillaud, C., Coppola, E., Pichelli, E., Sobolowski, S., Adinolfi, M., et al., 2021. The first multi-model ensemble of regional climate simulations at kilometer-scale resolution, part I: evaluation of precipitation. Clim. Dyn. https://doi.org/10.1007/s00382-021-05708-w.

Bermúdez, M., Ntegeka, V., Wolfs, V., Willems, P., 2018. Development and comparison of two fast surrogate models for urban pluvial flood simulations. Water Resour. Manage. 32 (8), 2801–2815. https://doi.org/10.1007/s11269-018-1959-8.

Bocanegra, R.A., Vallés-Morán, F.J., Francés, F., 2018. Review and analysis of vehicle stability models during floods and proposal for future improvements. J. Flood Risk Manage. 13, e12551 https://doi.org/10.1111/jfr3.12551.

Bucchignani, E., Mercogliano, P., Panitz, H.J., Montesarchio, M., 2018. Climate change projections for the Middle East-North Africa domain with COSMO-CLM at different spatial resolutions. Adv. Clim. Change Res. 9 (1), 66–80. https://doi.org/10.1016/j.accre.2018.01.004.

Cannon, A.J., Sobie, S.R., Murdock, T.Q., 2015. Bias correction of GCM precipitation by quantile mapping: how well do methods preserve changes in quantiles and extremes? J. Climatol. 28, 6938–6959. https://doi.org/10.1175/JCLI-D-14-00754.1.

Cao, R., Li, F., Feng, P., 2020. Exploring the hydrologic response to the urban building coverage ratio by model simulation. Theor. Appl. Climatol. 1–11 https://doi.org/10.1007/s00704-020-03139-x.

Cea, L., Bladé, E., 2015. A simple and efficient unstructured finite volume scheme for solving the shallow water equations in overland flow applications. Water Resour. Res. 51 (7), 5464–5486. https://doi.org/10.1002/2014WR016547.

Chen, W., Huang, G., Zhang, H., Wang, W., 2018. Urban inundation response to rainstorm patterns with a coupled hydrodynamic model: A case study in Haidian Island, China. J. Hydrol. 564, 1022–1035. https://doi.org/10.1016/j.jhydrol.2018.07.069.

Chow, V.T., Maidment, D.R., Mays, L.W., 1988. Applied Hydrology. McGraw-Hill, New York, USA.

Christiansen, B., 2020. Understanding the Distribution of Multimodel Ensembles, Journal of Climate, 33(21), 9447-9465. Retrieved Mar 18, 2021. 10.1175/JCLI-D-20-0186.1.

Cooley, D., 2013. Return Periods and Return Levels Under Climate Change. In: AghaKouchak A., Easterling D., Hsu K., Schubert S., Sorooshian S. (eds) Extremes in a Changing Climate. Water Science and Technology Library, vol 65. Springer, Dordrecht. 10.1007/978-94-007-4479-0_4.

Costabile, P., Costanzo, C., De Lorenzo, G., De Santis, R., Penna, N., Macchione, F., 2021. Terrestrial and airborne laser scanning and 2-D modelling for 3-D flood hazard maps in urban areas: new opportunities and perspectives. Environ. Modell. Software 135, 104889. https://doi.org/10.1016/j.envsoft.2020.104889.

Costabile, P., Costanzo, C., De Lorenzo, G., Macchione, F., 2020a. Is local flood hazard assessment in urban areas significantly influenced by the physical complexity of the hydrodynamic inundation model? J. Hydrol. 580, 124231 https://doi.org/10.1016/j.jhydrol.2019.124231.

Costabile, P., Costanzo, C., Ferraro, D., Macchione, F., Petaccia, G., 2020b. Performances of the new HEC-RAS version 5 for 2-D hydrodynamic-based rainfall-runoff simulations at basin scale: Comparison with a state-of-the art model. Water 12 (9), 3433. https://doi.org/10.3390/w12092326.

de Almeida, G.A., Bates, P., Ozdemir, H., 2018. Modelling urban floods at submetre resolution: challenges or opportunities for flood risk management? J. Flood Risk Manage. 11, S855–S865. https://doi.org/10.1111/jfr3.12276.

Dale, M., Luck, B., Fowler, H.J., Blenkinsop, S., Gill, E., Bennett, J., et al., 2015. New climate change rainfall estimates for sustainable drainage. Proceedings of the Institution of Civil Engineers-Engineering Sustainability 170 (4), 214–224. https://doi.org/10.1680/jensu.15.00030.

Donat, M.G., Lowry, A.L., Alexander, L.V., O'Gorman, P.A., Maher, N., 2016. More extreme precipitation in the world's dry and wet regions. Nat. Clim. Change 6 (5), 508–513. https://doi.org/10.1038/nclimate2941.

Evans, B., Chen, A.S., Djordjević, S., Webber, J., Gómez, A.G., Stevens, J., 2020. Investigating the Effects of Pluvial Flooding and Climate Change on Traffic Flows in Barcelona and Bristol. Sustainability 12 (6), 2330. https://doi.org/10.3390/su12062330.

Ferraro, D., Costabile, P., Costanzo, C., Petaccia, G., Macchione, F., 2020. A spectral analysis approach for the a priori generation of computational grids in the 2-D hydrodynamic-based runoff simulations at a basin scale. J. Hydrol. 582, 124508 https://doi.org/10.1016/j.jhydrol.2019.124508.

Forero-Ortiz, E., Martínez-Gomariz, E., Cañas Porcuna, M., 2020. A review of flood impact assessment approaches for underground infrastructures in urban areas: a

focus on transport systems. Hydrol. Sci. J. 65 (11), 1943–1955. https://doi.org/10.1080/02626667.2020.1784424.

Ghimire, B., Chen, A.S., Guidolin, M., Keedwell, E.C., Djordjević, S., Savić, D.A., 2013. Formulation of a fast 2D urban pluvial flood model using a cellular automata approach. J. Hydroinf. 15 (3), 676–686. https://doi.org/10.2166/hydro.2012.245.

Ghodsi, S.H., Zahmatkesh, Z., Goharian, E., Kerachian, R., Zhu, Z., 2020. Optimal design of low impact development practices in response to climate change. J. Hydrol. 580, 124266 https://doi.org/10.1016/j.jhydrol.2019.124266.

Gibson, M.J., Savić, D.A., Djordjević, S., Chen, A.S., Fraser, S., Watson, T., 2016. Accuracy and computational efficiency of 2D urban surface flood modelling based on cellular automata. Procedia Eng. 154, 801–810. https://doi.org/10.1016/j.proeng.2016.07.409.

Guidolin, M., Chen, A.S., Ghimire, B., Keedwell, E.C., Djordjević, S., Savić, D.A., 2016. A weighted cellular automata 2D inundation model for rapid flood analysis. Environ. Modell. Software 84, 378–394. https://doi.org/10.1016/j.envsoft.2016.07.008.

Gusain, A., Mohanty, M.P., Ghosh, S., Chatterjee, C., Karmakar, S., 2020. Capturing transformation of flood hazard over a large River Basin under changing climate using a top-down approach. Sci. Total Environ. 726, 138600 https://doi.org/10.1016/j.scitotenv.2020.138600.

Guo, K., Guan, M., Yu, D., 2021. Urban surface water flood modelling-a comprehensive review of current models and future challenges. Hydrol. Earth Syst. Sci. 25 (5), 2843–2860. https://doi.org/10.5194/hess-25-2843-2021.

Hammond, M.J., Chen, A.S., Djordjević, S., Butler, D., Mark, O., 2015. Urban flood impact assessment: A state-of-the-art review. Urban Water J. 12 (1), 14–29. https://doi.org/10.1080/1573062X.2013.857421.

He, J., Qiang, Y., Luo, H., Zhou, S., Zhang, L., 2020. A stress test of urban system flooding upon extreme rainstorms in Hong Kong. J. Hydrol. 125713 https://doi.org/10.1016/j.jhydrol.2020.125713.

Hlodversdottir, A.O., Bjornsson, B., Andradottir, H.O., Eliasson, J., Crochet, P., 2015. Assessment of flood hazard in a combined sewer system in Reykjavik city centre. Water Sci. Technol. 71 (10), 1471–1477. https://doi.org/10.2166/wst.2015.119.

Hosseinzadehtalaei, P., Tabari, H., Willems, P., 2020. Climate change impact on short-duration extreme precipitation and intensity–duration–frequency curves over Europe. J. Hydrol. 590, 125249 https://doi.org/10.1016/j.jhydrol.2020.125249.

IPCC, 2014: Climate Change 2014: Synthesis Report. Contribution of Working Groups I, II and III to the Fifth Assessment Report of the Intergovernmental Panel on Climate Change [Core Writing Team, R.K. Pachauri and L.A. Meyer (eds.)]. IPCC, Geneva, Switzerland, 151 pp.

Jacob, D., Teichmann, C., Sobolowski, S., Katragkou, E., Anders, I., Belda, M., et al., 2020. Regional climate downscaling over Europe: perspectives from the EURO-CORDEX community. Reg. Environ. Change 20 (2), 1–20. https://doi.org/10.1007/s10113-020-01606-9.

Kasmalkar, I.G., Serafin, K.A., Miao, Y., Avery Bick, I., Ortolano, L., Ouyang, D., Suckale, J., 2020. When floods hit the road: Resilience to flood-related traffic disruption in the San Francisco Bay Area and beyond. Science. Advances 6 (32), eaba2423. https://doi.org/10.1126/sciadv.aba2423.

Kaspersen, P.S., Halsnæs, K., 2017. Integrated climate change risk assessment: A practical application for urban flooding during extreme precipitation. Clim. Serv. 6, 55–64. https://doi.org/10.1016/j.cliser.2017.06.012.

Kaspersen, P.S., Høegh Ravn, N., Arnbjerg-Nielsen, K., Madsen, H., Drews, M., 2017. Comparison of the impacts of urban development and climate change on exposing European cities to pluvial flooding. Hydrol. Earth Syst. Sci. 21 (8), 4131–4147. https://doi.org/10.5194/hess-21-4131-2017.

Kourtis, I.M., Tsihrintzis, V.A., 2021. Adaptation of urban drainage networks to climate change: A review. Sci. Total Environ. 145431 https://doi.org/10.1016/j.scitotenv.2021.145431.

Kramer, M., Terheiden, K., Wieprecht, S., 2016. Safety criteria for the trafficability of inundated roads in urban floodings. Int. J. Disaster Risk Reduct. 17, 77–84. https://doi.org/10.1016/j.ijdrr.2016.04.003.

Li, Y., Gong, J., Niu, L., Sun, J., 2019. A physically based spatiotemporal method of analyzing flood impacts on urban road networks. Nat. Hazards 97 (1), 121–137. https://doi.org/10.1007/s11069-019-03630-3.

Li, X., Willems, P., 2020. A hybrid model for fast and probabilistic urban pluvial flood prediction. Water Resources Research 56(6), e2019WR025128. 10.1029/2019WR025128.

Löschner, L., Herrnegger, M., Apperl, B., Senoner, T., Seher, W., Nachtnebel, H.P., 2017. Flood risk, climate change and settlement development: a micro-scale assessment of Austrian municipalities. Reg. Environ. Change 17 (2), 311–322. https://doi.org/10.1007/s10113-016-1009-0.

Löwe, R., Urich, C., Domingo, N.S., Mark, O., Deletic, A., Arnbjerg-Nielsen, K., 2017. Assessment of urban pluvial flood risk and efficiency of adaptation options through simulations - A new generation of urban planning tools. J. Hydrol. 550, 355–367. https://doi.org/10.1016/j.jhydrol.2017.05.009.

Luu, C., Von Meding, J., Kanjanabootra, S., 2018. Assessing flood hazard using flood marks and analytic hierarchy process approach: A case study for the 2013 flood event in Quang Nam. Vietnam. Natural Hazards 90 (3), 1031–1050. https://doi.org/10.1007/s11069-017-3083-0.

Macchione, F., Costabile, P., Costanzo, C., De Lorenzo, G., 2019. Extracting quantitative data from non-conventional information for the hydraulic reconstruction of past urban flood events. A case study. J. Hydrol. 576, 443–465. https://doi.org/10.1016/j.jhydrol.2019.06.031.

Madsen, H., Lawrence, D., Lang, M., Martinkova, M., Kjeldsen, T.R., 2014. Review of trend analysis and climate change projections of extreme precipitation and floods in Europe. J. Hydrol. 519, 3634–3650. https://doi.org/10.1016/j.jhydrol.2014.11.003.

Mahmoud, S.H., Gan, T.Y., 2018. Urbanization and climate change implications in flood risk management: Developing an efficient decision support system for flood

susceptibility mapping. Sci. Total Environ. 636, 152–167. https://doi.org/10.1016/j.scitotenv.2018.04.282.

Maraun, D., Wetterhall, F., Ireson, A.M., Chandler, R.E., Kendon, E.J., Widmann, M., et al., 2010. Precipitation downscaling under climate change. Recent developments to bridge the gap between dynamical models and the end user. Rev. Geophys. 48, RG3003. https://doi.org/10.1029/2009RG000314.

Martínez-Gomariz, E., Locatelli, L., Guerrero, M., Russo, B., Martínez, M., 2019. Socio-economic potential impacts due to urban pluvial floods in Badalona (Spain) in a context of climate change. Water 11 (12), 2658. https://doi.org/10.3390/w11122658.

Mei, C., Liu, J., Wang, H., Li, Z., Yang, Z., Shao, W., et al., 2020. Urban flood inundation and damage assessment based on numerical simulations of design rainstorms with different characteristics. Science China Technological Sciences 63 (11), 2292–2304. https://doi.org/10.1007/s11431-019-1523-2.

Padulano, R., Reder, A., Rianna, G., 2019. An ensemble approach for the analysis of extreme rainfall under climate change in Naples (Italy). Hydrol. Process. 33 (14), 2020–2036. https://doi.org/10.1002/hyp.13449.

Palla, A., Colli, M., Candela, A., Aronica, G.T., Lanza, L.G., 2018. Pluvial flooding in urban areas: the role of surface drainage efficiency. J. Flood Risk Manage. 11, S663–S676. https://doi.org/10.1111/jfr3.12246.

Papalexiou, S.M., Montanari, A., 2019. Global and regional increase of precipitation extremes under global warming. Water Resour. Res. 55, 4901–4914. https://doi.org/10.1029/2018WR024067.

Papilloud, T., Röthlisberger, V., Loreti, S., Keiler, M., 2020. Flood exposure analysis of road infrastructure–Comparison of different methods at national level. Int. J. Disaster Risk Reduct. 47, 101548 https://doi.org/10.1016/j.ijdrr.2020.101548.

Pregnolato, M., Ford, A., Glenis, V., Wilkinson, S., Dawson, R., 2017. Impact of climate change on disruption to urban transport networks from pluvial flooding. J. Infrastruct. Syst. 23 (4), 04017015. https://doi.org/10.1061/(ASCE)IS.1943-555X.0000372.

Reder, A., Iturbide, M., Herrera, S., Rianna, G., Mercogliano, P., Gutiérrez, J.M., 2018. Assessing variations of extreme indices inducing weather-hazards on critical infrastructures over Europe—the INTACT framework. Clim. Change 148 (1), 123–138. https://doi.org/10.1007/s10584-018-2184-4.

Russo, B., Gómez, M., Macchione, F., 2013. Pedestrian hazard criteria for flooded urban areas. Natural hazards 69.1 (2013): 251-265. DOI 10.1007/s11069-013-0702-2.

Seager, R., Osborn, T.J., Kushnir, Y., Simpson, I.R., Nakamura, J., Liu, H., 2019. Climate variability and change of Mediterranean-type climates. J. Clim. 32 (10), 2887–2915. https://doi.org/10.1175/JCLI-D-18-0472.1.

Sanderson, B.M., Knutti, R., 2012. On the interpretation of constrained climate model ensembles. Geophys. Res. Lett. 39, L16708. https://doi.org/10.1029/2012GL052665.

Singh, P., Sinha, V.S.P., Vijhani, A., Pahuja, N., 2018. Vulnerability assessment of urban road network from urban flood. Int. J. Disaster Risk Reduct. 28, 237–250. https://doi.org/10.1016/j.ijdrr.2018.03.017.

Shadmehri Toosi, A., Doulabian, S., Ghasemi Tousi, E., Calbimonte, G.H., Alaghmand, S., 2020. Large-scale flood hazard assessment under climate change: A case study. Ecol. Eng. 147, 105765 https://doi.org/10.1016/j.ecoleng.2020.105765.

Sperotto, A., Torresan, S., Gallina, V., Coppola, E., Critto, A., Marcomini, A., 2016. A multi-disciplinary approach to evaluate pluvial floods risk under changing climate: The case study of the municipality of Venice (Italy). Sci. Total Environ. 562, 1031–1043. https://doi.org/10.1016/j.scitotenv.2016.03.150.

Tanaka, T., Kiyohara, K., Tachikawa, Y., 2020. Comparison of fluvial and pluvial flood risk curves in urban cities derived from a large ensemble climate simulation dataset: A case study in Nagoya. Japan. Journal of Hydrology 584, 124706. https://doi.org/10.1016/j.jhydrol.2020.124706.

Tebaldi, C., Smith, R.W., Nychka, D., Mearns, L.O., 2005. Quantifying uncertainty in projections of regional climate change: A Bayesian approach to the analysis of multi-model ensembles. J. Clim. 18, 1524–1540. https://doi.org/10.1175/JCLI3363.1.

Todini, E., 1988. Rainfall-runoff modeling – Past, present and future. J. Hydrol. 100 (1–3), 341–352. https://doi.org/10.1016/0022-1694(88)90191-6.

Tu, T., Ercan, A., Carr, K.J., Kavvas, M.L., Trinh, T., Ishida, K., et al., 2020. Coupling hydroclimate-hydraulic-sedimentation models to estimate flood inundation and sediment transport during extreme flood events under a changing climate. Sci. Total Environ. 740, 140117 https://doi.org/10.1016/j.scitotenv.2020.140117.

Tuel, A., Eltahir, E.A.B., 2020. Why is the Mediterranean a climate change hot spot? J. Clim. 33 (14), 5829–5843. https://doi.org/10.1175/JCLI-D-19-0910.1.

Van Ootegem, L., Verhofstadt, E., Van Herck, K., Creten, T., 2015. Multivariate pluvial flood damage models. Environ. Impact Assess. Rev. 54, 91–100. https://doi.org/10.1016/j.eiar.2015.05.005.

Viglione, A., Laio, F., Claps, P., 2007. A comparison of homogeneity tests for regional frequency analysis. Water Resour. Res. 43, W03428. https://doi.org/10.1029/2006WR005095.

Wang, Y., Chen, A.S., Fu, G., Djordjević, S., Zhang, C., Savić, D.A., 2018. An integrated framework for high-resolution urban flood modelling considering multiple information sources and urban features. Environ. Modell. Software 107, 85–95. https://doi.org/10.1016/j.envsoft.2018.06.010.

Webber, J.L., Booth, G., Gunasekara, R., Fu, G., Butler, D., 2019a. Validating a rapid assessment framework for screening surface water flood risk. Water Environ. J. 33 (3), 427–442. https://doi.org/10.1111/wej.12415.

Webber, J.L., Fletcher, T.D., Cunningham, L., Fu, G., Butler, D., Burns, M.J., 2019b. Is green infrastructure a viable strategy for managing urban surface water flooding? Urban Water J. 17 (7), 598–608. https://doi.org/10.1080/1573062X.2019.1700286.

Willems, P., Vrac, M., 2011. Statistical precipitation downscaling for small-scale hydrological impact investigations of climate change. J. Hydrol. 402, 193–205. https://doi.org/10.1016/j.jhydrol.2011.02.030.

WMO (2009) Guide to Hydrological Practices. Volume II: Management of Water Resources and Application of Hydrological Practices. WMO Report No. 168, 6th edn, World Meteorological Organization, Geneva, Switzerland, p. 302.

Wu, Z., Zhou, Y., Wang, H., Jiang, Z., 2020. Depth prediction of urban flood under different rainfall return periods based on deep learning and data warehouse. Sci. Total Environ. 716, 137077.

Xu, X., Wang, Y.-C., Kalcic, M., Muenich, R.L., Yang, Y.C.E., Scavia, D., 2019. Evaluating the impact of climate change on fluvial flood risk in a mixed-use watershed. Environ. Modell. Software 122, 104031. https://doi.org/10.1016/j.envsoft.2017.07.013.

Zhao, G., Pang, B., Xu, Z., Peng, D., Xu, L., 2019. Assessment of urban flood susceptibility using semi-supervised machine learning model. Sci. Total Environ. 659, 940–949. https://doi.org/10.1016/j.scitotenv.2018.12.217.

Zhou, Q., Leng, G., Huang, M., 2018. Impacts of future climate change on urban flood volumes in Hohhot in northern China: benefits of climate change mitigation and adaptations. Hydrol. Earth Syst. Sci. 22 (1), 305–316. https://doi.org/10.5194/hess-22-305-2018.

Zhou, Q., Leng, G., Su, J., Ren, Y., 2019. Comparison of urbanization and climate change impacts on urban flood volumes: Importance of urban planning and drainage adaptation. Sci. Total Environ. 658, 24–33. https://doi.org/10.1016/j.scitotenv.2018.12.184.

Zollo, A.L., Rillo, V., Bucchignani, E., Montesarchio, M., Mercogliano, P., 2016. Extreme temperature and precipitation events over Italy: assessment of high-resolution simulations with COSMO-CLM and future scenarios. Int. J. Climatol. 36 (2), 987–1004. https://doi.org/10.1002/joc.4401.